Isogeometric analysis of the isothermal Navier-Stokes-Korteweg equations

Hector Gomez[1] *, Thomas J.R. Hughes[2], Xesús Nogueira[1] and
Victor M. Calo[3]

1: Group of Numerical Methods in Engineering
University of A Coruña
Department of Mathematical Methods
Campus de Elviña, s/n
15192, A Coruña

2: Institute for Computational Engineering and Sciences
The University of Texas at Austin
1 University Station, C0200
201 E. 24th Street, Austin, TX 78712

3: King Abdullah University of Science and Technology
Earth and Environmental Science and Engineering
Applied Mathematics and Computational Science
4700 King Abdullah University of Science and Technology
Thuwal 23955-6900, Kingdom of Saudi Arabia

Abstract

This paper is devoted to the numerical simulation of the Navier-Stokes-Korteweg equations, a phase-field model for water/water-vapor two-phase flows. We develop a numerical formulation based on isogeometric analysis that permits straightforward treatment of the higher-order partial-differential operator that represents capillarity. We introduce a new refinement methodology that desensitizes the numerical solution to the computational mesh and achieves mesh invariant solutions. Finally, we present several numerical examples in two and three dimensions that illustrate the effectiveness and robustness of our approach.

Key words: Navier-Stokes-Korteweg, Vaporization, Condensation, Phase-field, Isogeometric Analysis

---

* Correspondence to: University of A Coruña, Deparment of Mathematical Methods
  Email address: `hgomez@udc.es` (Hector Gomez[1]).

1 Introduction

1.1 *Phase-transition phenomena: the phase-field approach*

There are two main different approaches to describe phase transition phenomena: *sharp-interface* models and *phase-field* (diffuse-interface) models. From a conceptual point of view, the straightforward approach is the use of sharp-interface models, which leads to moving boundary problems. These require the simultaneous resolution of the partial differential equations that hold in each phase and the boundary conditions on the interfaces [5,21,52]. The sharp-interface description has been a successful approach in a wide range of situations, but it leads to mathematical models whose numerical treatment is extremely complex.

Phase-field models provide an alternative description for phase-transition phenomena. The key idea in the phase-field approach is to replace sharp interfaces by thin transition regions where the interfacial forces are smoothly distributed [1]. The transition regions are part of the solution of the governing equations and, thus, front tracking is avoided. Phase-field models can be derived from classical irreversible thermodynamics [32]. Utilizing asymptotic expansions for vanishing interface thickness, it can be shown that classical sharp-interface models, including physical laws at interfaces are recovered [30,31]. For phase-field models to be realistic, the transition regions (diffuse interfaces) have to be extremely thin.

The use of diffuse-interface models to describe interfacial phenomena dates back to Korteweg [48] (1901), Cahn and Hilliard [13,14] (1958), and Landau and Ginzburg [49] (1965). Lately, the phase-field method has been used to model foams [27], ferroelectric ceramics [38,50], solidification [11,47,55], dendritic flow [45,46], microstructure evolution in solids [29], planet formation [60], cancer growth [28], and liquid-liquid interfaces [54]. The diversity of areas where the phase-field approach has been successfully used is striking. One of the most recent and significant achievements using this methodology is the development of a mathematical model that explains, apparently for the first time, why preferential flow occurs during infiltration into homogeneous and dry soil [15,16]. For recent reviews of phase-field methods the reader is referred to [9,17,20,26].

This paper is devoted to the numerical simulation of the Navier-Stokes-Korteweg equations, a phase-field model for water/water-vapor two-phase flows. The current form of the Navier-Stokes-Korteweg equations is the result of many contributions. The starting point is the classical theory of capillarity originated by Gibbs [34]. Later, Korteweg [48] introduced a constitutive equation

for the Cauchy stress tensor that included density gradients. The advances in the theory of capillarity attained by van der Waals [61] were also fundamental. In his paper [61], van der Waals introduced the concept of continuous variation of density, which leads to the diffuse-interface representation of the liquid-vapor flow. Finally, Dunn and Serrin [24] introduced the concept of interstitial working and rearranged the energy balance equation so that the complete model satisfies the second law of thermodynamics.

In this paper we focus on the isothermal version of the Navier-Stokes-Korteweg equations. Although constant temperature may seem a very strong hypothesis for this model, that is not the case in a wide variety of situations. Some of the numerical examples in this paper were computed using both the isothermal and the full Navier-Stokes-Korteweg equations and we found negligible variations in temperature.

1.2 Numerical formulations for the Navier-Stokes-Korteweg equations

The problem of water/water-vapor two-phase flow has attracted the attention of many prominent researchers over the years. The Navier-Stokes-Korteweg equations constitute the most commonly accepted mathematical model for this physical problem and may have a significant potential in representing phenomena of engineering interest, such as cavitation. However, there are very few numerical solutions to the Navier-Stokes-Korteweg equations in the literature. We refer the reader to [43], where the authors propose a finite difference method. Another significant work (probably, the most comprehensive to date) was carried out by Diehl [23], who proposed a discontinuous Galerkin formulation.

We feel that one of the main reasons for the absence of numerical solutions in the literature is that the Navier-Stokes-Korteweg equations involve third-order partial differential spatial operators. This fact significantly limits the use of conforming finite element methods. The reason for this is third-order operators necessitate basis functions that are piecewise smooth and $\mathcal{C}^1$-continuous globally. There are a very limited number of two-dimensional finite elements possessing $\mathcal{C}^1$ continuity applicable to complex geometries, but none in three dimensions. Another important aspect is that the Navier-Stokes-Korteweg equations include a length scale which represents the thickness of the liquid-vapor interfaces. For the Navier-Stokes-Korteweg equations to be a realistic model, the length scale (that is, the thickness of the interfaces) must be extremely small. This length scale must be resolved by the computational mesh, which constitutes a challenge for any numerical method. Several researchers have tried to modify the Navier-Stokes-Korteweg equations in such a way that the interfaces are enlarged without affecting important magnitudes on the in-

terface, such as, for example, surface tension. Probably, the most successful attempt to date was proposed by Jamet [42], but we feel that there is still opportunity for improvement.

In this paper, we propose a numerical formulation for the Navier-Stokes-Korteweg equations based on isogeometric analysis. Isogeometric analysis is a generalization of finite element analysis possessing several advantages [6,7,10,19,25,35,40,41,53]. We feel that isogeometric analysis presents a unique combination of attributes that can be exploited on problems involving higher-order partial-differential operators, namely, higher-order accuracy, robustness, two- and three-dimensional geometric flexibility, compact support, and, most importantly, $\mathcal{C}^1$ and higher-order continuity. The simplicity of isogeometric analysis compared with many procedures that have been published in the literature is noteworthy. These properties open the way to application to phase-field models, as shown in the previous work of the authors on the Cahn-Hilliard equation [35,36] (for another study that uses conforming finite elements for phase-field models, see [58,59]). We believe that isogeometric analysis may prove an effective procedure for solving problems of these kinds on complex geometries.

To address the treatment of problems in which the length scale of the model is unresolved by the computational mesh, we propose a new scaling for the parameters of the Navier-Stokes-Korteweg equations. One of the key ideas is to adapt the length scale of the Navier-Stokes-Korteweg equations to the computational mesh. Thus, as the mesh is refined, the length scale of the model tends to its correct value, which is of the order of magnitude of ten Angstroms. This scaling turned out to be crucial to perform reliable computations.

Finally, we present several numerical examples in two and three dimensions which illustrate the effectiveness and robustness of our approach.

2 The isothermal Navier-Stokes-Korteweg equations

2.1 Continuous problem in strong form

Let $\Omega \subset \mathbb{R}^d$ be an open set, where d is the number of spatial dimensions. The boundary of Ω, assumed sufficiently smooth, is denoted Γ. We call $\boldsymbol{n}$ the unit outward normal to Γ. The initial/boundary value problem can be stated as: find the density $\rho : \overline{\Omega} \times (0, T) \mapsto (0, b)$ and the velocity $\boldsymbol{u} : \overline{\Omega} \times (0, T) \mapsto \mathbb{R}^3$

such that

$$\frac{\partial \rho}{\partial t} + \nabla \cdot (\rho \boldsymbol{u}) = 0 \qquad \text{in} \quad \Omega \times (0, T), \quad (1.1)$$

$$\frac{\partial (\rho \boldsymbol{u})}{\partial t} + \nabla \cdot (\rho \boldsymbol{u} \otimes \boldsymbol{u} + p\boldsymbol{I}) - \nabla \cdot \boldsymbol{\tau} - \nabla \cdot \boldsymbol{\varsigma} = \rho \boldsymbol{f} \qquad \text{in} \quad \Omega \times (0, T), \quad (1.2)$$

$$\boldsymbol{u} = 0 \qquad \text{on} \quad \Gamma \times (0, T), \quad (1.3)$$

$$\nabla \rho \cdot \boldsymbol{n} = 0 \qquad \text{on} \quad \Gamma \times (0, T), \quad (1.4)$$

$$\boldsymbol{u}(\boldsymbol{x}, 0) = \boldsymbol{u}_0(\boldsymbol{x}) \qquad \text{in} \quad \overline{\Omega}, \quad (1.5)$$

$$\rho(\boldsymbol{x}, 0) = \rho_0(\boldsymbol{x}) \qquad \text{in} \quad \overline{\Omega}. \quad (1.6)$$

where $\boldsymbol{u}_0 : \overline{\Omega} \mapsto \mathbb{R}^3$, $\rho_0 : \overline{\Omega} \mapsto (0, b)$ are given functions which represent the initial density and velocity, respectively. The rest of the notation is as follows: $\boldsymbol{f}$ is the body force per unit mass and $\boldsymbol{\tau}$ is the viscous stress tensor. We consider Newtonian fluids, that is,

$$\boldsymbol{\tau} = \overline{\mu}(\nabla \boldsymbol{u} + \nabla^T \boldsymbol{u}) + \overline{\lambda} \nabla \cdot \boldsymbol{u}\, \boldsymbol{I} \qquad (2)$$

where $\overline{\mu}$ and $\overline{\lambda}$ are the viscosity coefficients and $\boldsymbol{I}$ is the identity tensor. $\boldsymbol{\varsigma}$ is the so-called Korteweg tensor, defined as

$$\boldsymbol{\varsigma} = \lambda \left(\rho \Delta \rho + \frac{1}{2} |\nabla \rho|^2 \right) \boldsymbol{I} - \lambda \nabla \rho \otimes \nabla \rho. \qquad (3)$$

Finally, p is the thermodynamic pressure, defined as,

$$p = Rb\frac{\rho \theta}{b - \rho} - a\rho^2 \qquad (4)$$

Equation (4) is known as van der Waals equation, and gives the pressure in terms of density and temperature, which for the isothermal model is assumed to be constant. When modeling liquid-vapor flows, the van der Waals equation is the most commonly employed model, but there are certainly other possibilities. Prime examples are the equations proposed by Berthelot [4], Kamerlingh-Onnes, Beattie-Bridgeman, Wilson [62] and more recently Serrin [57].

The pressure p is a non-monotone function of ρ for certain combinations of temperature and density. Actually, the sign of

$$p_\rho \equiv \frac{\partial p}{\partial \rho}(\rho, \theta) = Rb^2 \frac{\theta}{(b - \rho)^2} - 2a\rho \qquad (5)$$

in the physically relevant interval, that is $\rho \in (0, b)$, may be analyzed using well-known properties of cubic polynomials. Let us define

$$\theta_c = \frac{8}{27}\frac{ab}{R}. \qquad (6)$$

Then,

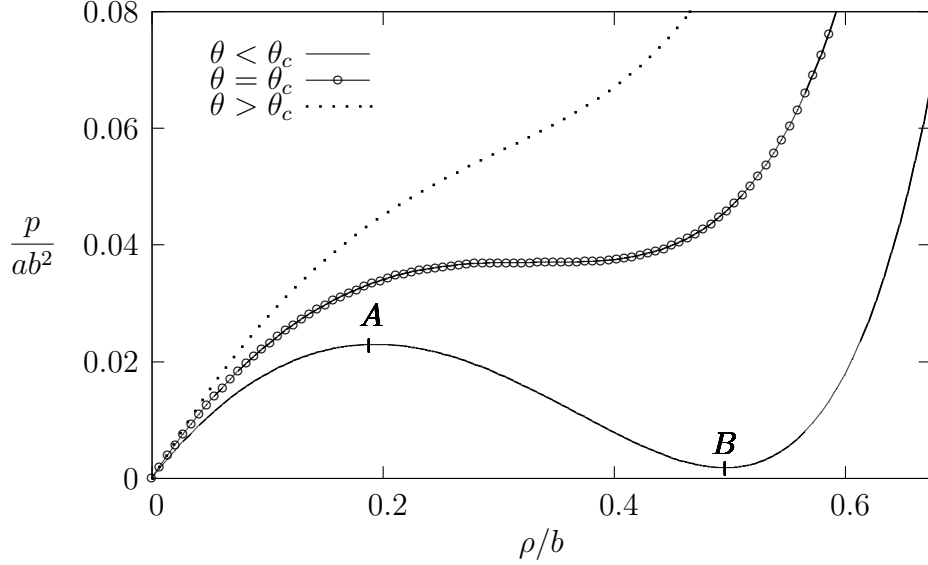Fig. 1. Van der Waals pressure as a function of density for $\theta < \theta_c$, $\theta = \theta_c$ and $\theta > \theta_c$. The pressure is a non-monotone function of density for $\theta < \theta_c$.

(1) For $\theta > \theta_c$, $p_\rho > 0 \ \forall \rho \in (0, b)$.
(2) For $\theta < \theta_c$, the equation $p_\rho = 0$ has two roots, ρ_v and ρ_l (we assume that $\rho_v < \rho_l$). The sign of p_ρ is given by $p_\rho < 0 \ \forall \rho \in (\rho_v, \rho_l)$; $p_\rho > 0 \ \forall \rho \in [0, \rho_v) \cup (\rho_l, b)$. Observe that ρ_v and ρ_l only depend on θ/θ_c and may be exactly calculated as the roots of a cubic polynomial.
(3) For $\theta = \theta_c$, the two roots ρ_v and ρ_l merge at a single point which constitutes a double root of the equation $p_\rho = 0$. At any other point in $(0, b)$, $p_\rho > 0$.

On the basis of the above argument we call θ_c the *critical temperature*. This is the maximum temperature at which two-phase flow is stable. We represent typical van der Waals pressure profiles in Figure 1. The portion AB of the isotherm plotted as a solid line corresponds to the region where $p_\rho < 0$. Without any regularizing effect, this region would correspond to unstable states which would immediately degenerate into a mixture of liquid and vapor phases. However, the Navier-Stokes-Korteweg equations do include a regularizing term. Mathematically, this term is represented by a partial-differential operator acting on the density. With this regularizing term, the region AB corresponds to the interface between water and water-vapor. The thickness of the interfaces is given by a length scale of the model. This point will be further analyzed in sections 4.1 and 4.2.

Remarks:

(1) The existence and uniqueness of solution for the initial/boundary value problem defined in (1) has been proven in [22].
(2) We wish to emphasize the difference between λ and $\overline{\lambda}$. The former is the
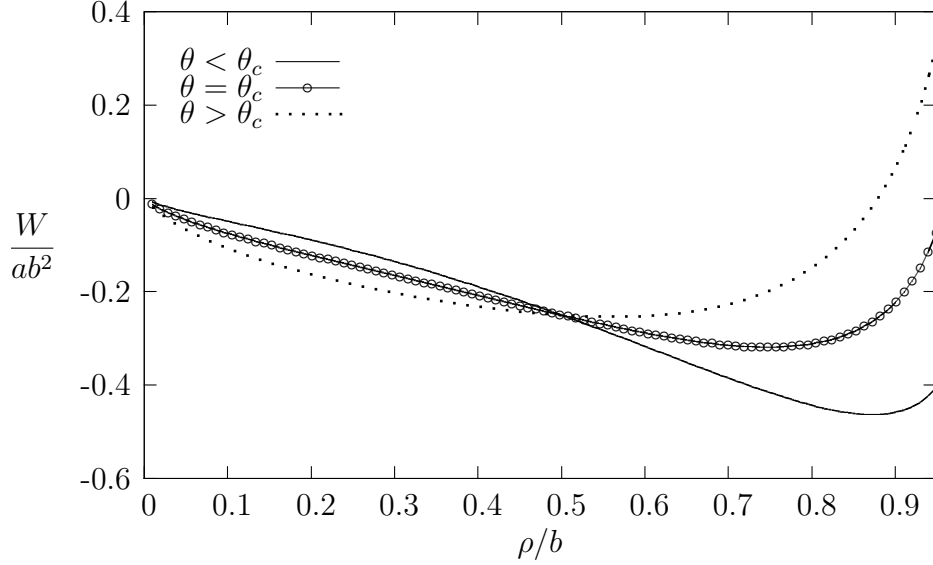
6

Fig. 2. Potential W as a function of density for $\theta < \theta_c$, $\theta = \theta_c$ and $\theta > \theta_c$. The potential W is a non-convex function of density for $\theta < \theta_c$.

    capillarity coefficient while the latter is one of the viscosity coefficients.

(3) The capillarity term in equation (1.2) may be written in non-conservative form using the relationship

$$\nabla \cdot \boldsymbol{\varsigma} = \lambda \rho \nabla (\Delta \rho). \tag{7}$$

2.2 Nonlinear stability of the isothermal Navier-Stokes-Korteweg equations

The fundamental stability property of the isothermal Navier-Stokes-Korteweg equations is expressed in terms of the free-energy

$$\mathcal{E}(\rho, \rho\boldsymbol{u}) = \int_\Omega \left(W(\rho) + \frac{\lambda}{2} |\nabla\rho|^2 + \frac{1}{2}\rho|\boldsymbol{u}|^2 \right) \mathrm{d}\boldsymbol{x} \tag{8}$$

where $W(\rho)$ is a potential that satisfies the relationship

$$\rho W''(\rho) = p_\rho. \tag{9}$$

Thus, $W(\rho)$ is given by

$$W(\rho) = R\theta\rho \log\left(\frac{\rho}{b - \rho} \right) - a\rho^2. \tag{10}$$

Equation (9) indicates that W is a non-convex function of density when $p_\rho < 0$. In Figure 2 we present plots of the potential W as a function of density for $\theta < \theta_c$, $\theta = \theta_c$ and $\theta > \theta_c$.

The energy functional $\mathcal{E}$ constitutes a Lyapunov functional. To prove this we define the real-valued function $\epsilon : \mathbb{R}^+ \mapsto \mathbb{R}$ as

$$\epsilon(t) = \mathcal{E}\left(\rho(\cdot, t), \rho\boldsymbol{u}(\cdot, t)\right) \quad \forall t > 0. \tag{11}$$

Then, using the chain rule, we obtain

$$\frac{\mathrm{d}\epsilon}{\mathrm{d}t} = \int_\Omega \left(\mathcal{E}_\rho \frac{\partial\rho}{\partial t} + \mathcal{E}_{\rho\boldsymbol{u}} \frac{\partial(\rho\boldsymbol{u})}{\partial t}\right)\mathrm{d}\boldsymbol{x} \tag{12}$$

where $\mathcal{E}_\rho$ and $\mathcal{E}_{\rho\boldsymbol{u}}$ represent the variational derivatives of the functional $\mathcal{E}$ with respect to its first and second slot, respectively. Using the standard definition of variational derivative, we obtain

$$\mathcal{E}_\rho = W'(\rho) - \lambda\Delta\rho - \frac{1}{2}|\boldsymbol{u}|^2 \tag{13.1}$$

$$\mathcal{E}_{\rho\boldsymbol{u}} = \boldsymbol{u} \tag{13.2}$$

Using (13), (1.1) and (1.2) we can rewrite (12) as

$$\begin{aligned}
\frac{\mathrm{d}\epsilon}{\mathrm{d}t} = &-\int_\Omega \nabla \cdot (\rho\boldsymbol{u})W'(\rho)\mathrm{d}\boldsymbol{x} + \int_\Omega \lambda\nabla \cdot (\rho\boldsymbol{u})\Delta\rho\,\mathrm{d}\boldsymbol{x} + \frac{1}{2}\int_\Omega \nabla \cdot (\rho\boldsymbol{u})|\boldsymbol{u}|^2\mathrm{d}\boldsymbol{x} \\
&- \int_\Omega \boldsymbol{u} \cdot \nabla \cdot (\rho\boldsymbol{u} \otimes \boldsymbol{u})\mathrm{d}\boldsymbol{x} - \int_\Omega \boldsymbol{u} \cdot \nabla p + \int_\Omega \boldsymbol{u} \cdot \nabla \cdot \boldsymbol{\tau}\,\mathrm{d}\boldsymbol{x} \\
&+ \int_\Omega \lambda\rho\boldsymbol{u} \cdot \nabla(\Delta\rho)\mathrm{d}\boldsymbol{x} + \int_\Omega \rho\boldsymbol{f} \cdot \boldsymbol{u}\,\mathrm{d}\boldsymbol{x}
\end{aligned} \tag{14}$$

Taking into account (1.3), the relationship $\rho W''(\rho) = p_\rho$ and integrating by parts, we obtain

$$\frac{\mathrm{d}\epsilon}{\mathrm{d}t} = -\int_\Omega \boldsymbol{\tau} : \nabla\boldsymbol{u}\,\mathrm{d}\boldsymbol{x} + \int_\Omega \rho\boldsymbol{f} \cdot \boldsymbol{u}\,\mathrm{d}\boldsymbol{x} \tag{15}$$

For $\overline{\mu} \geq 0$, $\overline{\lambda} + \frac{2}{3}\overline{\mu} \geq 0$

$$\frac{\mathrm{d}\epsilon}{\mathrm{d}t} \leq \int_\Omega \rho\boldsymbol{f} \cdot \boldsymbol{u}\,\mathrm{d}\boldsymbol{x}. \tag{16}$$

Finally, if we assume $\boldsymbol{f} = 0$, we obtain

$$\frac{\mathrm{d}\epsilon}{\mathrm{d}t} \leq 0 \tag{17}$$

which proves that $\mathcal{E}$ constitutes a Lyapunov functional.

8

3   Numerical formulation for the isothermal Navier-Stokes-Korteweg equations

In this section we develop a numerical formulation for the isothermal Navier-Stokes-Korteweg equations (we will assume vanishing body forces). We use isogeometric analysis for the spatial discretization, which allows us to generate the $\mathcal{C}^1$-continuous functions that are needed for the discretization of the third-order partial-differential operator in primal form. We integrate in time using the generalized-α method. We also make use of an adaptive time stepping scheme previously proposed by the authors [35].

3.1   Continuous problem in the weak form

Let X denote both the trial solution and weighting function spaces, which are assumed to be identical. At this point, we consider periodic boundary conditions in all directions. Let $(\cdot, \cdot)_\Omega$ denote the $\mathcal{L}^2$ inner product with respect to the domain Ω. Taking into account all of this, the variational formulation is stated as follows:

Find $\mathbf{U} = \{\rho, \boldsymbol{u}\} \in \mathsf{X}$ such that $\forall \mathbf{W} = \{q, \boldsymbol{w}\} \in \mathsf{X}$:

$$\mathsf{B}(\mathbf{W}, \mathbf{U}) = 0 \tag{18}$$

with

$$
\begin{aligned}
\mathsf{B}(\mathbf{W}, \mathbf{U}) = &\left(q, \frac{\partial \rho}{\partial t}\right)_\Omega + \left(\boldsymbol{w}, \boldsymbol{u}\frac{\partial \rho}{\partial t}\right)_\Omega + \left(\boldsymbol{w}, \rho\frac{\partial \boldsymbol{u}}{\partial t}\right)_\Omega \\
&- (\nabla q, \rho\boldsymbol{u})_\Omega - (\nabla \boldsymbol{w}, \rho\boldsymbol{u} \otimes \boldsymbol{u})_\Omega - (\nabla \cdot \boldsymbol{w}, p)_\Omega + (\nabla \boldsymbol{w}, \boldsymbol{\tau})_\Omega \\
&- (\nabla \nabla \cdot \boldsymbol{w}, \lambda\rho\nabla\rho)_\Omega - (\nabla \cdot \boldsymbol{w}, \lambda\nabla\rho \cdot \nabla\rho)_\Omega \\
&- (\nabla(\nabla\rho \cdot \boldsymbol{w}), \lambda\nabla\rho)_\Omega
\end{aligned}
\tag{19}
$$

The repeated integration by parts of equation (19) under the assumptions of sufficient regularity leads to the Euler-Lagrange form of (19)

$$
\left(q, \frac{\partial \rho}{\partial t}\right)_\Omega + (q, \nabla \cdot (\rho\boldsymbol{u}))_\Omega + \left(\boldsymbol{w}, \frac{\partial(\rho\boldsymbol{u})}{\partial t}\right)_\Omega + (\boldsymbol{w}, \nabla \cdot (\rho\boldsymbol{u} \otimes \boldsymbol{u}))_\Omega + (\boldsymbol{w}, \nabla p)_\Omega
$$

$$
- (\boldsymbol{w}, \nabla \cdot \boldsymbol{\tau})_\Omega - (\boldsymbol{w}, \lambda\rho\nabla(\Delta\rho))_\Omega = 0 \tag{20}
$$

which implies the weak satisfaction of equations (1.1) and (1.2).

3.2 The semidiscrete formulation

For the space discretization of (19) we make use of the Galerkin method. We approximate (19) by the following variational problem over the finite element spaces: find $\mathbf{U}^h = \{\rho^h, \boldsymbol{u}^h\} \in \mathsf{X}^h \subset \mathsf{X}$ such that $\forall \mathbf{W}^h = \{q^h, \boldsymbol{w}^h\} \in \mathsf{X}^h \subset \mathsf{X}$

$$B(\mathbf{W}^h, \mathbf{U}^h) = 0 \tag{21}$$

where $\mathbf{W}^h$ and $\mathbf{U}^h$ are defined as

$$\mathbf{W}^h = \{q^h, \boldsymbol{w}^h\}, \ q^h = \sum_{A=1}^{n_b} q_A N_A, \ \boldsymbol{w}^h = \sum_{A=1}^{n_b} \boldsymbol{w}_A N_A, \tag{22.1}$$

$$\mathbf{U}^h = \{\rho^h, \boldsymbol{u}^h\}, \ \rho^h = \sum_{A=1}^{n_b} \rho_A N_A, \ \boldsymbol{u}^h = \sum_{A=1}^{n_b} \boldsymbol{u}_A N_A. \tag{22.2}$$

In (22), the N_A's are the basis functions, and n_b is the dimension of the discrete space. Note that the condition $\mathsf{X}^h \subset \mathsf{X}$ mandates our discrete space to be at least $\mathcal{H}^2$-conforming. This requirement is satisfied by a NURBS (Non Uniform Rational B-Splines) basis of $\mathcal{C}^1$-continuity or higher.

3.3 Time discretization and numerical implementation

We integrate in time using the generalized-α method. This method was originally derived in [18] for the equations of structural dynamics and subsequently applied to turbulence computations in [2,8,44] and to the Cahn-Hilliard phase-field model in [35,36].

3.3.1 Time stepping scheme

Let A be the control point index. We denote by $\boldsymbol{e}_i$ the ith cartesian basis vector. Let $\mathbf{V}$ and $\dot{\mathbf{V}}$ denote the vector of global degrees of freedom and its time derivative, respectively. We define the following residual vectors:

$$\mathbf{R}^\mathsf{C} = \{\mathsf{R}_A^\mathsf{C}\} \tag{23.1}$$

$$\mathsf{R}_A^\mathsf{C} = B(\{N_A, 0\}, \{\rho^h, \boldsymbol{u}^h\}) \tag{23.2}$$

$$\mathbf{R}^\mathsf{M} = \{\mathsf{R}_{Ai}^\mathsf{M}\} \tag{23.3}$$

$$\mathsf{R}_{Ai}^\mathsf{M} = B(\{0, N_A \boldsymbol{e}_i\}, \{\rho^h, \boldsymbol{u}^h\}) \tag{23.4}$$

$$\mathbf{R} = \{\mathbf{R}^\mathsf{C}, \mathbf{R}^\mathsf{M}\} \tag{23.5}$$

10

The algorithm can be written as: given $\dot{\mathbf{V}}_n$, $\mathbf{V}_n$ and $\Delta t_n = t_{n+1} - t_n$, find $\dot{\mathbf{V}}_{n+1}$, $\mathbf{V}_{n+1}$, $\mathbf{V}_{n+\alpha_m}$, $\mathbf{V}_{n+\alpha_f}$ such that

$$\mathbf{R}^C(\dot{\mathbf{V}}_{n+\alpha_m}, \mathbf{V}_{n+\alpha_f}) = 0, \tag{24.1}$$

$$\mathbf{R}^M(\dot{\mathbf{V}}_{n+\alpha_m}, \mathbf{V}_{n+\alpha_f}) = 0, \tag{24.2}$$

$$\mathbf{V}_{n+1} = \mathbf{V}_n + \Delta t_n \dot{\mathbf{V}}_n + \gamma \Delta t_n(\dot{\mathbf{V}}_{n+1} - \dot{\mathbf{V}}_n), \tag{24.3}$$

$$\dot{\mathbf{V}}_{n+\alpha_m} = \dot{\mathbf{V}}_n + \alpha_m(\dot{\mathbf{V}}_{n+1} - \dot{\mathbf{V}}_n), \tag{24.4}$$

$$\mathbf{V}_{n+\alpha_f} = \mathbf{V}_n + \alpha_f(\mathbf{V}_{n+1} - \mathbf{V}_n). \tag{24.5}$$

where Δt_n is the current time step size and α_m, α_f and γ are real-valued parameters that define the method. Parameters α_m, α_f and γ are selected based on considerations of accuracy and stability. Jansen, Whiting and Hulbert proved in [44] that, for a model problem, second-order accuracy in time is achieved if

$$\gamma = \frac{1}{2} + \alpha_m - \alpha_f, \tag{25}$$

while unconditional stability is attained if

$$\alpha_m \geq \alpha_f \geq 1/2. \tag{26}$$

Parameters α_m and α_f can be parametrized in terms of ϱ_∞, the spectral radius of the amplification matrix as $\Delta t \to \infty$, as

$$\alpha_m = \frac{1}{2}\left(\frac{3 - \varrho_\infty}{1 + \varrho_\infty}\right), \ \alpha_f = \frac{1}{1 + \varrho_\infty} \tag{27}$$

Setting γ according to (25), a family of second-order accurate and unconditionally stable time integration schemes is defined in terms of the parameter $\varrho_\infty \in [0, 1]$ which controls high-frequency dissipation [39].

The non-linear system of equations (24) is approximated by using Newton's method which leads to a two-stage predictor-multicorrector algorithm.

Predictor stage: Set

$$\mathbf{V}_{n+1,(0)} = \mathbf{V}_n, \tag{28.1}$$

$$\dot{\mathbf{V}}_{n+1,(0)} = \frac{\gamma - 1}{\gamma} \dot{\mathbf{V}}_n. \tag{28.2}$$

where the subscript 0 on the left-hand side quantities is the iteration index of the nonlinear solver. This predictor was shown to be effective for turbulence applications [8,44] and for the Cahn-Hilliard phase-field model [35].

Multicorrector stage: Repeat the following steps for $i = 1, 2, \ldots, i_{max}$

(1) Evaluate iterates at the α-levels

$$\dot{\mathbf{V}}_{n+\alpha_m,(i)} = \dot{\mathbf{V}}_n + \alpha_m(\dot{\mathbf{V}}_{n+1,(i-1)} - \dot{\mathbf{V}}_n), \qquad (29.1)$$

$$\mathbf{V}_{n+\alpha_f,(i)} = \mathbf{V}_n + \alpha_f(\mathbf{V}_{n+1,(i-1)} - \mathbf{V}_n). \qquad (29.2)$$

(2) Use the solutions at the α-levels to assemble the residual and the tangent matrix of the linear system

$$\mathbf{K}_{(i)}\Delta\dot{\mathbf{V}}_{n+1,(i)} = -\mathbf{R}_{(i)} \qquad (30)$$

Solve this linear system using a preconditioned GMRES algorithm (see Saad and Shultz [56]) to a specified tolerance.

(3) Use $\Delta\dot{\mathbf{V}}_{n+1,(i)}$ to update the iterates as

$$\dot{\mathbf{V}}_{n+1,(i)} = \dot{\mathbf{V}}_{n+1,(i-1)} + \Delta\dot{\mathbf{V}}_{n+1,(i)}, \qquad (31.1)$$

$$\mathbf{V}_{n+1,(i)} = \mathbf{V}_{n+1,(i-1)} + \gamma\Delta t_n\Delta\dot{\mathbf{V}}_{n+1,(i)}. \qquad (31.2)$$

This completes one nonlinear iteration.

The nonlinear iterative algorithm should be repeated until both residual vectors $\mathbf{R}^C$ and $\mathbf{R}^M$ have been reduced to a given tolerance. In transient computations, we reduce both residuals to 10^{-3} or 10^{-4} of its initial value. The tangent matrix in equation (30) is given by

$$\mathbf{K} = \frac{\partial\mathbf{R}(\dot{\mathbf{V}}_{n+\alpha_m}, \mathbf{V}_{n+\alpha_f})}{\partial\dot{\mathbf{V}}_{n+\alpha_m}}\frac{\partial\dot{\mathbf{V}}_{n+\alpha_m}}{\partial\dot{\mathbf{V}}_{n+1}} + \frac{\partial\mathbf{R}(\dot{\mathbf{V}}_{n+\alpha_m}, \mathbf{V}_{n+\alpha_f})}{\partial\mathbf{V}_{n+\alpha_f}}\frac{\partial\mathbf{V}_{n+\alpha_f}}{\partial\dot{\mathbf{V}}_{n+1}}$$

$$= \alpha_m\frac{\partial\mathbf{R}(\dot{\mathbf{V}}_{n+\alpha_m}, \mathbf{V}_{n+\alpha_f})}{\partial\dot{\mathbf{V}}_{n+\alpha_m}} + \alpha_f\gamma\Delta t_n\frac{\partial\mathbf{R}(\dot{\mathbf{V}}_{n+\alpha_m}, \mathbf{V}_{n+\alpha_f})}{\partial\mathbf{V}_{n+\alpha_f}} \qquad (32)$$

where the iteration index i has been omitted to simplify the notation.

Remarks:

(1) The value $\varrho_\infty = 0.5$ has proved an effective choice for turbulence computations [8] and for the Cahn-Hilliard phase-field model [35]. We adopted this value for all the computations presented in this paper.

(2) We used the consistent tangent matrix in our computations. Two to four nonlinear iterations are typically required to reduce the nonlinear residual to 10^{-3} of its initial value in a time step. The solution of system (30) to a tolerance of 10^{-3} requires normally 30 to 40 GMRES iterations using a diagonal preconditioner.

Like that of other phase-field models, the solution of the Navier-Stokes-Korteweg equations experiences fast variations in time due to strong changes in its topology. This fact makes the use of time-step size adaptivity attractive. We use the algorithm proposed by the authors in [35].

4   A new paradigm for refinement of the Navier-Stokes-Korteweg equations

There is a very limited number of numerical solutions to the Navier-Stokes-Korteweg equations in the literature (to the best of our knowledge the most complete study to date is [23]). One of the main reasons for this is Navier-Stokes-Korteweg equations are only a realistic model if the thickness of the interfaces is extremely small. The interfaces must be resolved by the computational mesh, which imposes severe restrictions on any numerical method. In this paper we propose a new paradigm for refinement according to which the thickness of the interfaces is adapted to the computational mesh. We tested this approach on several examples and found a consistent and significant improvement over the standard methodology. To introduce the refinement methodology we begin by deriving a dimensionless form of the Navier-Stokes-Korteweg equations.

4.1   Dimensionless form of the Navier-Stokes-Korteweg equations

In order to simplify the exposition we will assume for the reminder of the paper that the Stokes hypothesis is satisfied, that is,

$$\overline{\lambda} = -\frac{2}{3}\overline{\mu}. \tag{33}$$

All the physical quantities involved in the Navier-Stokes-Korteweg equations can be measured using units of measurement that belong to the $MLT\Theta$ class, in which units of mass, length, time and temperature are chosen as fundamental units. Due to the fundamental principle which states that physical laws do not depend on arbitrarily chosen units of measurement [3], we can rescale length, mass, time and temperature by arbitrary positive numbers. Let us scale the units of measurement of length by L_0, mass by bL_0^3, time by $L_0/\sqrt{ab}$ and temperature by θ_c. Let us denote by $\hat{\phi}$ the value of the physical quantity ϕ in the new system of units. Thus, the Navier-Stokes-Korteweg equations in

the new system of units read as:

$$\frac{\partial \widehat{\rho}}{\partial \widehat{t}} + \widehat{\nabla} \cdot (\widehat{\rho}\widehat{\boldsymbol{u}}) = 0 \tag{34.1}$$

$$\frac{\partial (\widehat{\rho}\widehat{\boldsymbol{u}})}{\partial \widehat{t}} + \widehat{\nabla} \cdot (\widehat{\rho}\widehat{\boldsymbol{u}} \otimes \widehat{\boldsymbol{u}} + \widehat{p}\boldsymbol{I}) - \frac{1}{\text{Re}}\widehat{\nabla} \cdot \widehat{\boldsymbol{\tau}} - \text{Ca}^2 \widehat{\rho}\widehat{\nabla}(\widehat{\Delta}\widehat{\rho}) = 0 \tag{34.2}$$

$$\widehat{p} = \frac{8}{27}\frac{\widehat{\theta}\widehat{\rho}}{1 - \widehat{\rho}} - \widehat{\rho}^2 \tag{34.3}$$

$$\widehat{\boldsymbol{\tau}} = \widehat{\nabla}\widehat{\boldsymbol{u}} + \widehat{\nabla}^T\widehat{\boldsymbol{u}} - \frac{2}{3}\widehat{\nabla} \cdot \widehat{\boldsymbol{u}}\boldsymbol{I} \tag{34.4}$$

where

$$\text{Re} = \frac{L_0 b\sqrt{ab}}{\overline{\mu}} \quad \text{and} \quad \text{Ca} = \frac{\sqrt{\lambda/a}}{L_0} \tag{35}$$

are the Reynolds number and the capillarity number, respectively.

Likewise, the dimensionless free energy is defined as

$$\widehat{\mathcal{E}}(\widehat{\rho}, \widehat{\rho}\widehat{\boldsymbol{u}}) = \mathcal{E}(\rho, \rho\boldsymbol{u})(L_0^3 ab^2)^{-1} = \int_{\widehat{\Omega}} \left(\widehat{W}(\widehat{\rho}) + \frac{1}{2}\text{Ca}^2|\widehat{\nabla}\widehat{\rho}|^2 + \frac{1}{2}|\widehat{\boldsymbol{u}}|^2 \right) \text{d}\widehat{\boldsymbol{x}} \tag{36}$$

where

$$\widehat{W}(\widehat{\rho}) = \frac{8}{27}\widehat{\theta}\widehat{\rho}\log\left(\frac{\widehat{\rho}}{1 - \widehat{\rho}}\right) - \widehat{\rho}^2. \tag{37}$$

In what follows we will use the dimensionless form of the Navier-Stokes-Korteweg equations. For notational simplicity we will omit the hats on the dimensionless variables.

4.2   Refinement methodology

The capillarity number defined in (35) expresses the ratio between a characteristic length scale of the Navier-Stokes-Korteweg equations and the arbitrary length scale L_0. This suggests that Ca is related to the thickness of the interfaces. We performed a number of one-dimensional numerical simulations which indicated that Ca scales as the thickness of the interfaces.

We propose a refinement methodology that adapts the thickness of the interfaces to the computational mesh. We think of Ca as a regularizing parameter that should be as small as possible (we are assuming that the interfaces are always unresolved by the computational mesh, which unfortunately, is a very realistic hypothesis). The parameter Ca is linearly scaled to the mesh, so the phase-field model converges to its corresponding sharp-interface model as we refine the grid. The ultimate objective of this methodology is to obtain the

best approximation to the sharp-interface model for a given mesh. This concept has already been successfully used by the authors for the Cahn-Hilliard phase-field model [35].

Therefore, we propose to scale the capillarity number as

$$\text{Ca} = \frac{h}{L_0} \tag{38}$$

where h is a characteristic length scale of the spatial mesh. Equation (35) and fundamental arguments from dimensional analysis imply that the product of Re and Ca must be a constant. Thus, we propose to scale Re as

$$\text{Re} = \alpha \text{Ca}^{-1} \tag{39}$$

where $\alpha = b\sqrt{b\lambda}/\overline{\mu}$ is a constant whose magnitude is of the order of one for typical values of b, λ and $\overline{\mu}$ (see [23]). Using the scaling (38) for the capillarity number, we obtain

$$\text{Re} = \alpha \frac{L_0}{h} \tag{40}$$

which shows that the Reynolds number must be also adapted to the computational mesh.

We illustrate the proposed methodology with an example. For this example we take

$$\alpha = 2 \tag{41}$$

$$h = \frac{1}{2} \max_i \sqrt{A_i} \tag{42}$$

where A_i is the area of the ith element of the computational mesh.

In this example we start the computation with a non-equilibrium solution and let the simulation evolve until the steady state is reached. Our computational domain is $\overline{\Omega} = [0,1] \times [0,1]$. Boundary conditions are doubly periodic and we use $\mathcal{C}^1$ quadratic elements. For the temperature, we take the value $\theta = 0.85$. In Figure 3, we compare the solutions using the standard refinement methodology (refine the mesh, while the constitutive parameters are kept constant) with the solutions using the proposed refinement methodology (the constitutive parameters are adapted to the mesh). On the right hand side of Figure 3, the parameters Re and Ca are adapted to the computational mesh using scalings (38), (39), (41) and (42). On the left hand side of Figure 3, only the mesh changes from top to bottom and the parameters Re and Ca remain fixed to the value that corresponds to an uniform mesh comprised of 256^2 elements. On the top row, the mesh is 64^2, on the second row, the mesh is 128^2 and on the bottom row, the mesh is 256^2. We observe that the proposed refinement

methodology significantly reduces the mesh dependence of the solution. The only difference between the solutions on the right hand side of Figure 3 is the thickness of the interface.

In Figures 4 and 5 we plot cutlines of the solutions obtained using both methodologies. The cutlines correspond to the steady state solutions for $y = 0.5$ on different meshes. In both cases, we sample the solution at knots and plot it using piecewise linear interpolation. Figure 4 corresponds to the standard approach and Figure 5 to the proposed methodology. The proposed approach is clearly superior to the standard refinement methodology. In Figure 5 the solutions are monotone and the layers are captured in an accurate and stable way.

This example shows the potential of the proposed approach to successfully deal with problems where the characteristic length scale of the continuous phase-field model is unresolved by the computational mesh. We believe that with this technique phase-field modeling, which has been used heretofore primarily in scientific studies, may become a practical engineering technology.

Remarks:

(1) The scaling (39) that we impose to keep the solution invariant under mesh refinement has been repeatedly suggested by the physics community [51]. They derived the scaling (39) by studying the existence and stability of traveling wave solutions of the Korteweg-de Vries and modified Korteweg-de Vries equations [37].

(2) The idea that higher-order terms of phase-field models must fulfill a scaling relationship with lower-order terms seems to be growing in the phase-field community. For another study suggesting so, see [15].

5   Numerical examples for the isothermal Navier-Stokes-Korteweg equations

In this section we present several numerical examples in two and three dimensions, including static and dynamic equilibrium phenomena.

For all the examples we select the physical parameters Ca and Re using the scaling (38), (39) and (41) with $L_0 = 1$. For the characteristic length of the mesh we do not take the value (42), but a safer choice. We use the value

$$h = \max_i V_i^{1/d} \tag{43}$$

where d is the number of spatial dimensions of the problem and V_i is the volume $(d = 3)$ or area $(d = 2)$ of the ith element of the computational mesh.
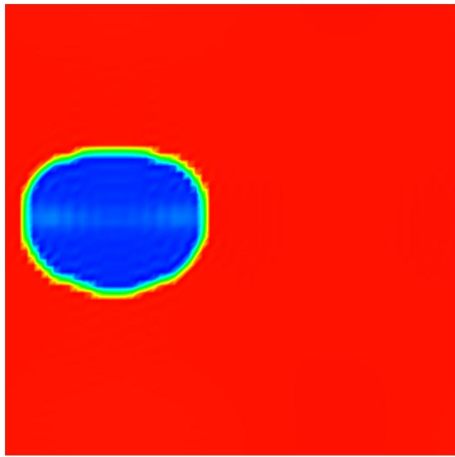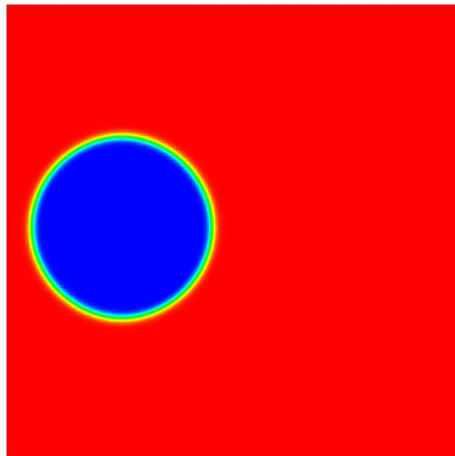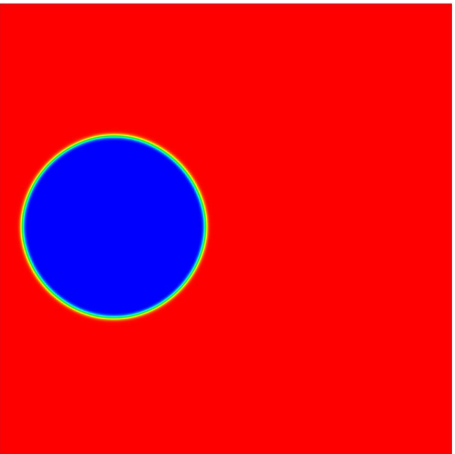
(a) Standard. The mesh is 64^2
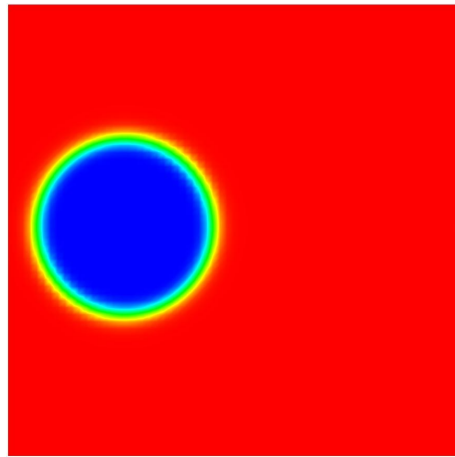
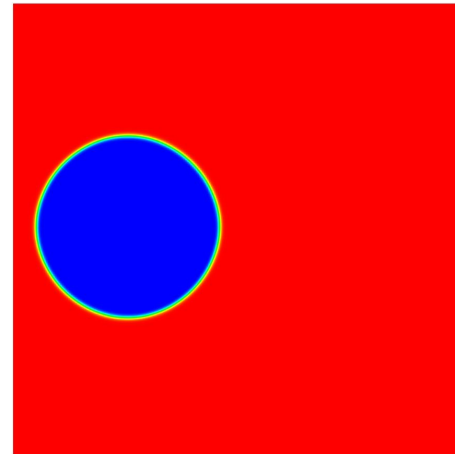(b) Proposed. The mesh is 64^2
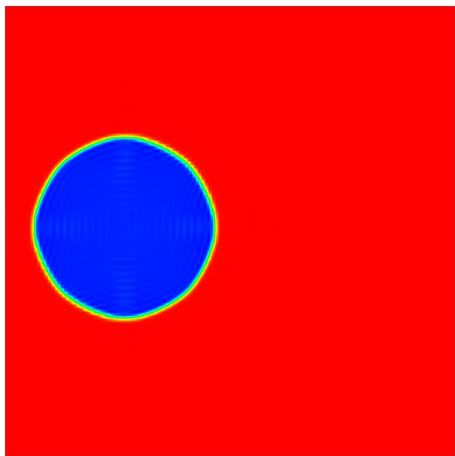
(c) Standard. The mesh is 128^2

(d) Proposed. The mesh is 128^2

(e) Standard. The mesh is 256^2

(f) Proposed. The mesh is 256^2

Fig. 3. Comparison of the proposed and standard refinement techniques. We plot steady state solutions of a model problem on uniform meshes comprised of 64^2 (a)–(b), 128^2 (c)–(d) and 256^2 (e)–(f) $\mathcal{C}^1$ quadratic elements. On the left-hand side we plot the solution using the same parameters Re and Ca for all meshes. The dependence of the solution on the mesh size is apparent. On the right-hand side we plot the solutions adapting Re and Ca to the resolution of the computational mesh. The topology of the solution is invariant with respect to the mesh size. The only difference in the solutions on the right-hand side is the thickness of the interfaces.
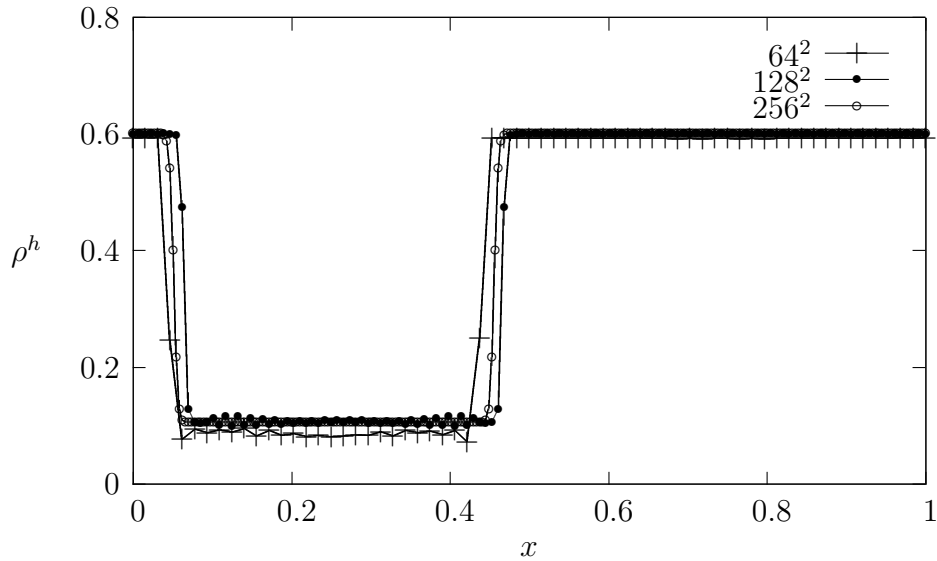
Fig. 4. Cutlines (restrictions to the line $y = 0.5$) of the solutions presented on the left-hand side of Figure 3. We sample the solution at knots and plot it using piecewise linear interpolation. Symbols in the plot correspond to knot locations. The solutions correspond to the standard refinement methodology (Re and Ca are independent of the mesh size). The dependence of the solution on the mesh size is apparent.
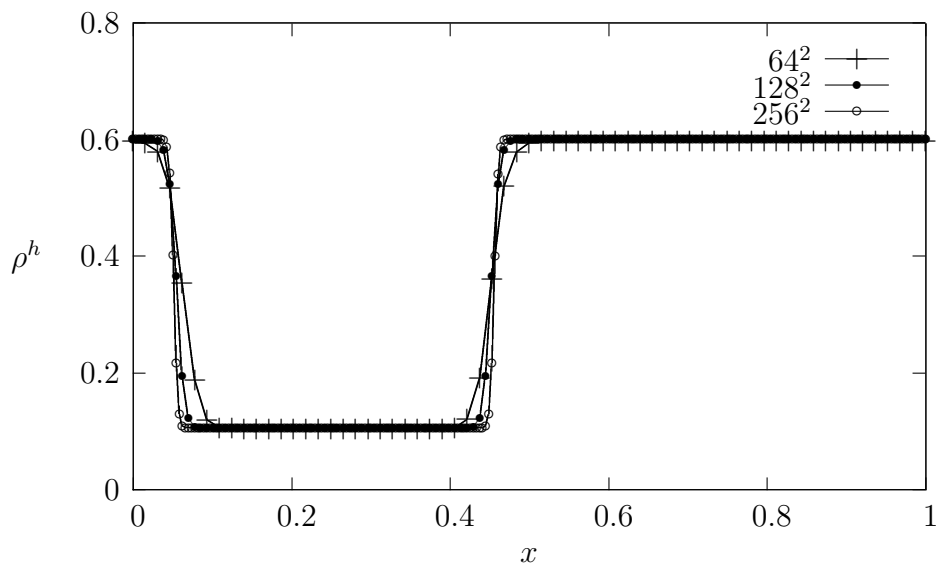
Fig. 5. Cutlines (restrictions to the line $y = 0.5$) of the solutions presented on the right-hand side of Figure 3. We sample the solution at knots and plot it using piecewise linear interpolation. Symbols in the plot correspond to knot locations. The solutions correspond to the new refinement methodology (Re and Ca scale with the mesh size). All the solutions are monotone and the only difference between them is the thickness of the interfaces.

The fact that we use the same scaling for all the examples shows the robustness of our approach.

We use the value $\theta = 0.85$ for the temperature in all the computations. This value leads to a non-monotone pressure profile that makes two-phase flow possible.

We also use $\mathcal{C}^1$ quadratic elements for all the examples.

5.1 Evolution to static equilibrium in two dimensions

In this example we present the evolution of three vapor bubbles toward static equilibrium. Our computational domain is the square $\overline{\Omega} = [0, 1] \times [0, 1]$. We use periodic boundary conditions in all directions. We employ a uniform mesh comprised of 256^2 $\mathcal{C}^1$-quadratic elements.

At the initial time, we set three vapor bubbles at points $C_1 = (0.75, 0.50)$, $C_2 = (0.25, 0.50)$ and $C_3 = (0.40, 0.75)$. The radii of the bubbles are $R_1 = 0.10$, $R_2 = 0.15$ and $R_3 = 0.08$, respectively. We regularize the interfaces using hyperbolic tangent profiles. Thus, the initial condition for the density may be written as,

$$\rho_0(\boldsymbol{x}) = -0.15 + 0.25 \left[\tanh\left(\frac{d_1(\boldsymbol{x}) - R_1}{2\mathrm{Ca}} \right) + \tanh\left(\frac{d_2(\boldsymbol{x}) - R_2}{2\mathrm{Ca}} \right) + \tanh\left(\frac{d_3(\boldsymbol{x}) - R_3}{2\mathrm{Ca}} \right) \right]$$
(44)

where $d_i(\boldsymbol{x})$ is the Euclidean distance between $\boldsymbol{x}$ and C_i, $i = 1, 2, 3$. The value of the initial density ranges approximately from 0.1 to 0.6. These values are close to the equilibrium states for the water-vapor and water phases, respectively. The initial condition is plotted in Figure 6(a). We set a zero velocity field at the initial time.

We know from classical physics that the equilibrium of a vapor bubble in an isothermal and isobaric system is unstable [12]. In this example, the larger bubble sets the equilibrium pressure. Under that pressure, the smaller bubbles are unstable and, as a consequence, vanish. The larger bubble evolves to a static equilibrium. The dynamic process can be observed in Figure 6, where the evolution of density is depicted. In Figure 7 we plot the evolution of the pressure. Although for a given time, the pressure ranges approximately from $1.838 \cdot 10^{-3}$ to $2.298 \cdot 10^{-2}$, the extreme values are reached within the interfaces and, as a consequence, are not physically relevant. We are primarily interested in the pressure difference between the vapor and liquid phases, which is very small compared to the whole range of variation of the pressure (at the steady state the pressure inside the bubble is approximately $1.85455 \cdot 10^{-2}$, while outside the bubble it is approximately $1.78861 \cdot 10^{-2}$). For this reason, we use
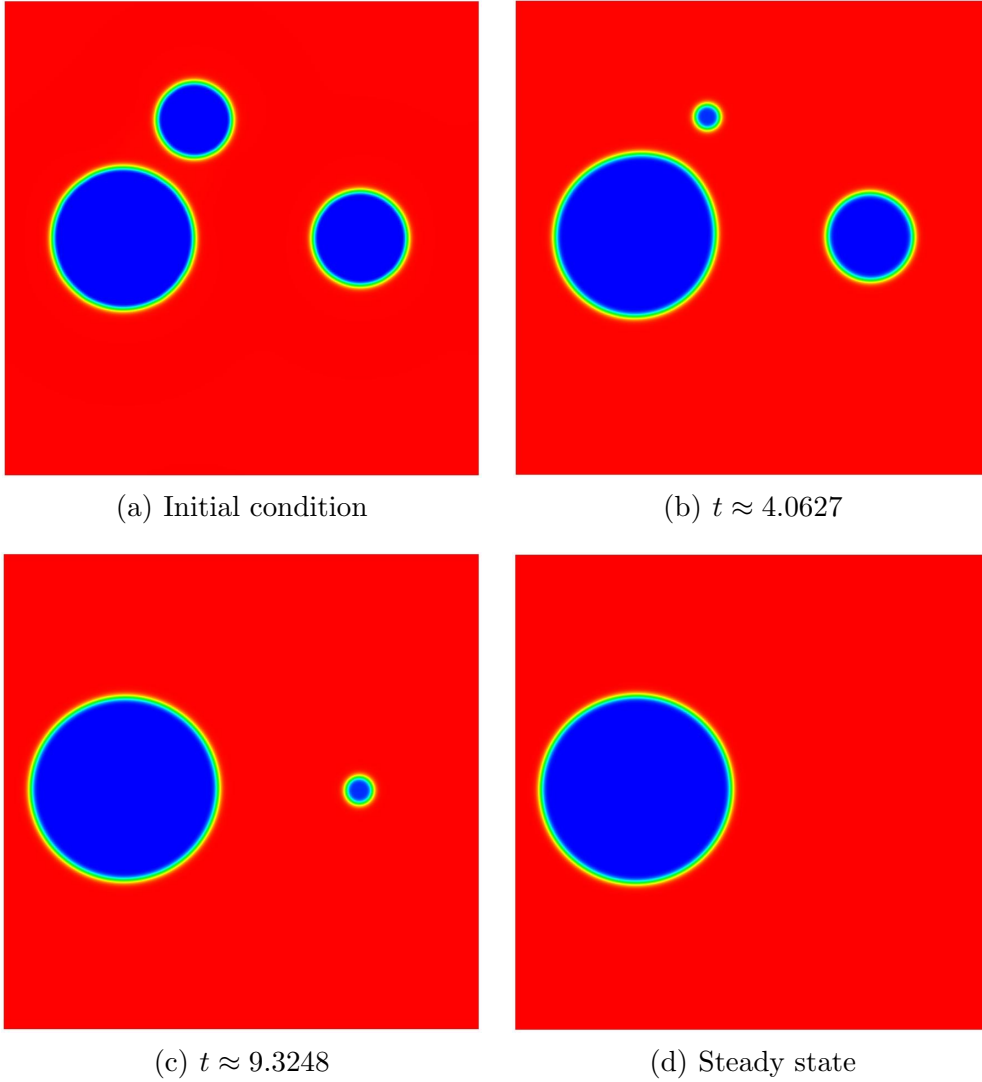
(a) Initial condition   (b) $t \approx 4.0627$

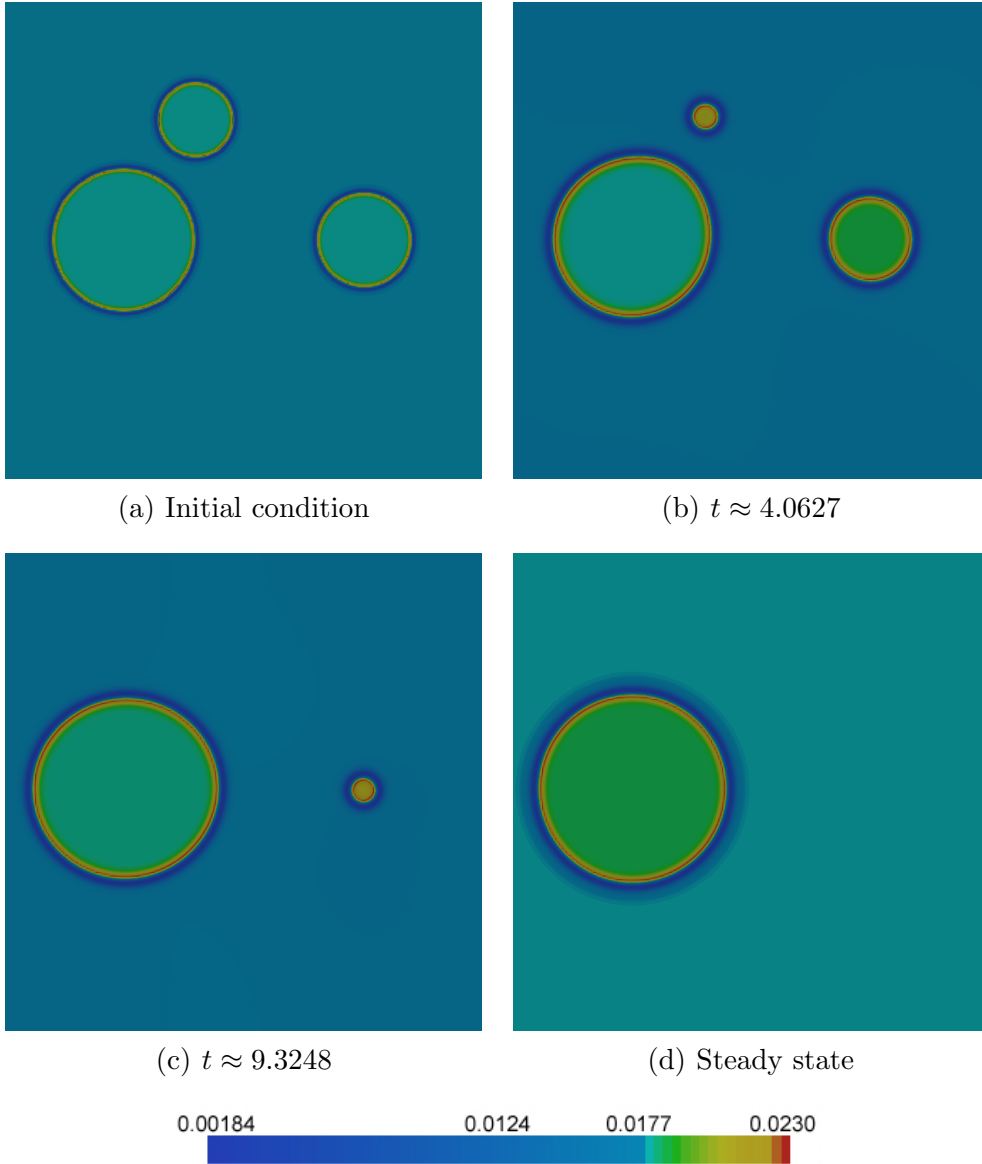(c) $t \approx 9.3248$ (d) Steady state

Fig. 6. Evolution of the density from an initial condition with three vapor bubbles. The mesh is comprised of 256^2 $\mathcal{C}^1$-quadratic elements.

a non-uniform color scale to plot the pressure. In Figure 7 we observe that smaller bubbles have higher inside pressures, which is the expected result.

In Figure 8 we plot the evolution in time of the free energy. There are two significant variations of the free energy that correspond to the times at which the smaller bubbles vanish. The free energy is decreasing for all times, which indicates that our numerical scheme is performing well. Diehl reported in [23] that most numerical schemes lead to non-monotone energy profiles.

In Figure 9 we plot the evolution of the time step size. The time step size ranges over an order of magnitude, which makes the use of adaptivity attractive. We observe two significant variations of the time step size that correspond to the times at which the smaller bubbles vanish. At those times, the time step is reduced by an order of magnitude, reflecting that a significant physical event

Fig. 7. Evolution of the pressure from an initial condition with three vapor bubbles. The mesh is comprised of 256^2 $\mathcal{C}^1$-quadratic elements.

(the disappearance of a bubble) is taking place.

Remarks:

(1) The assumption of constant temperature is adequately accurate for this problem. We ran this example using the non-isothermal equations and found negligible variations of the temperature both in space and time.

(2) Numerical solutions to a similar problem can be found in [23], where a discontinuous Galerkin formulation is employed. Our solutions are at least of the same quality as those reported in [23].

(3) Our time stepping-scheme enabled us to integrate the equations for very
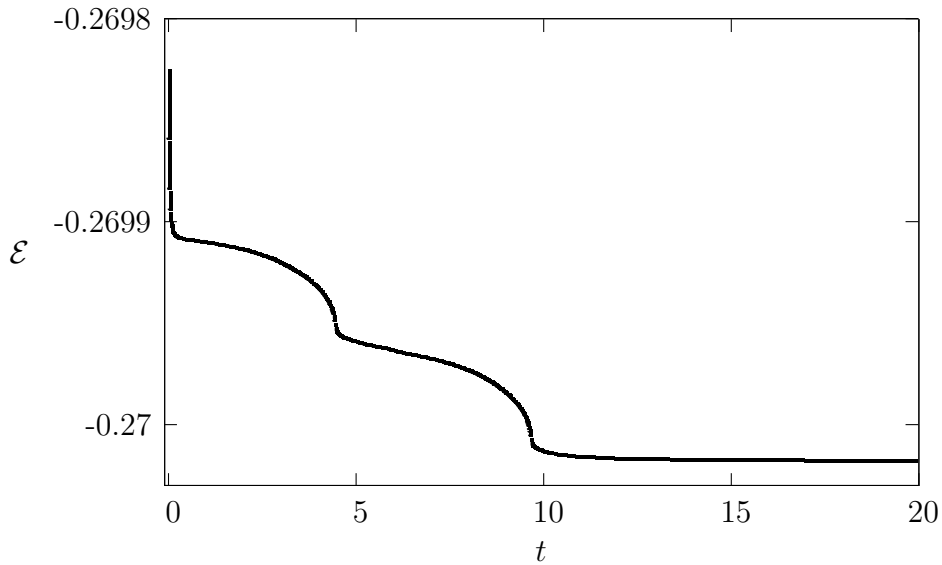
Fig. 8. Static equilibrium in two dimensions. Evolution of the free energy. There are two significant variations of the free energy that correspond to the times at which the smaller bubbles vanish. The free-energy is decreasing for all times. The mesh is comprised of 256^2 $\mathcal{C}^1$-quadratic elements.
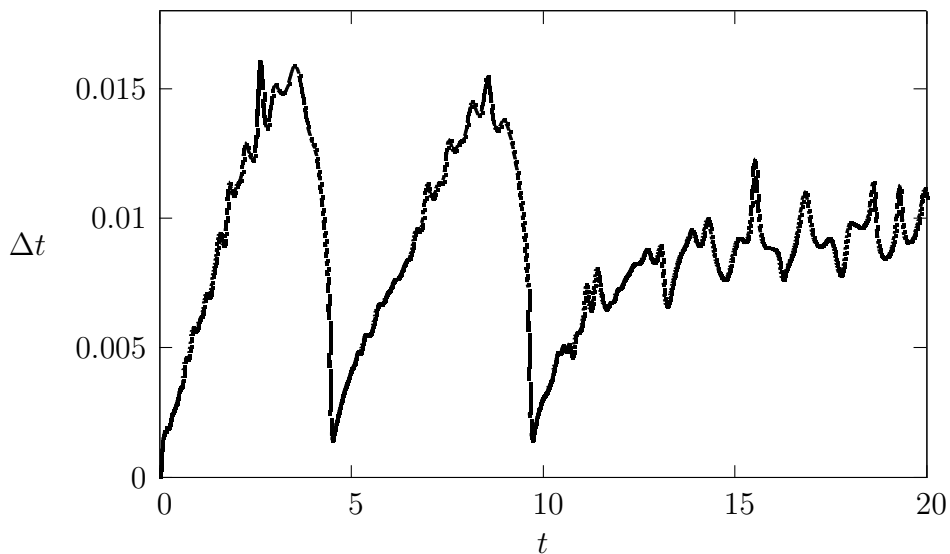
Fig. 9. Static equilibrium in two dimensions. Evolution of the time step. There are two significant variations that correspond to the times at which the smaller bubbles vanish. The mesh is comprised of 256^2 $\mathcal{C}^1$-quadratic elements.

long times, where the solutions where considered steady, at a reasonable computational cost. However, we plot the evolution of the free energy and the time step size only up to much earlier times in order to make the presentation clearer. This is done throughout the paper.

22

5.2 Coalescence of two bubbles in two dimensions

The previous example illustrated the behavior of several vapor bubbles when they are far away from each other. We observed that the smaller bubbles vanish because they are unstable under the pressure imposed by the largest bubble. When two vapor bubbles are close enough (at a distance of the order of magnitude of the thickness of the interfaces) the process is different. Both bubbles merge into a single vapor region that evolves to a circular shape with the equilibrium curvature.

To simulate this physical phenomenon we set two vapor bubbles at the initial time. The centers of the bubbles are located at points $C_1 = (0.40, 0.50)$ and $C_2 = (0.78, 0.50)$. Their radii are $R_1 = 0.25$ and $R_2 = 0.10$, respectively. We regularize the interfaces using hyperbolic tangent profiles, which leads to the initial condition for the density

$$\rho_0(\boldsymbol{x}) = 0.10 + 0.25 \left[\tanh\left(\frac{d_1(\boldsymbol{x}) - R_1}{2\mathrm{Ca}} \right) + \tanh\left(\frac{d_2(\boldsymbol{x}) - R_2}{2\mathrm{Ca}} \right) \right] \qquad (45)$$

where again $d_i(\boldsymbol{x})$ is the Euclidean distance between $\boldsymbol{x}$ and C_i, $i = 1, 2$, and the values of the density range approximately from 0.1 to 0.6. The initial condition is plotted in Figure 10(a). The velocity field at the initial time is set to zero.

In Figure 10, we plot the evolution of density in time. This solution shows the ability of the model to represent fast variations in the topology of the solution.

Figure 11 shows the evolution of the pressure (we use again a non-uniform color scale). We observe that when the two bubbles coalesce (Figure 11(b)) the smaller one has a larger inside pressure. That pressure difference drives the fast topology variation that happens afterwards (this is in agreement with the current knowledge about bubble coalescence; see, for example, [33].) At the steady state the pressure inside the bubble is approximately $1.85825 \cdot 10^{-2}$, while outside the bubble it is $1.81005 \cdot 10^{-2}$.

In Figure 12 we plot the evolution in time of the free energy. Again, the free energy at the discrete level is monotone. The most significant variation corresponds to the time at which the two bubbles merge. In Figure 13 we plot the evolution of the time step size.

Remark:

According to the Young-Laplace equation, the pressure difference between the vapor and liquid phases at equilibrium is inversely proportional to the radii of the bubbles. The proportionality constant depends only on
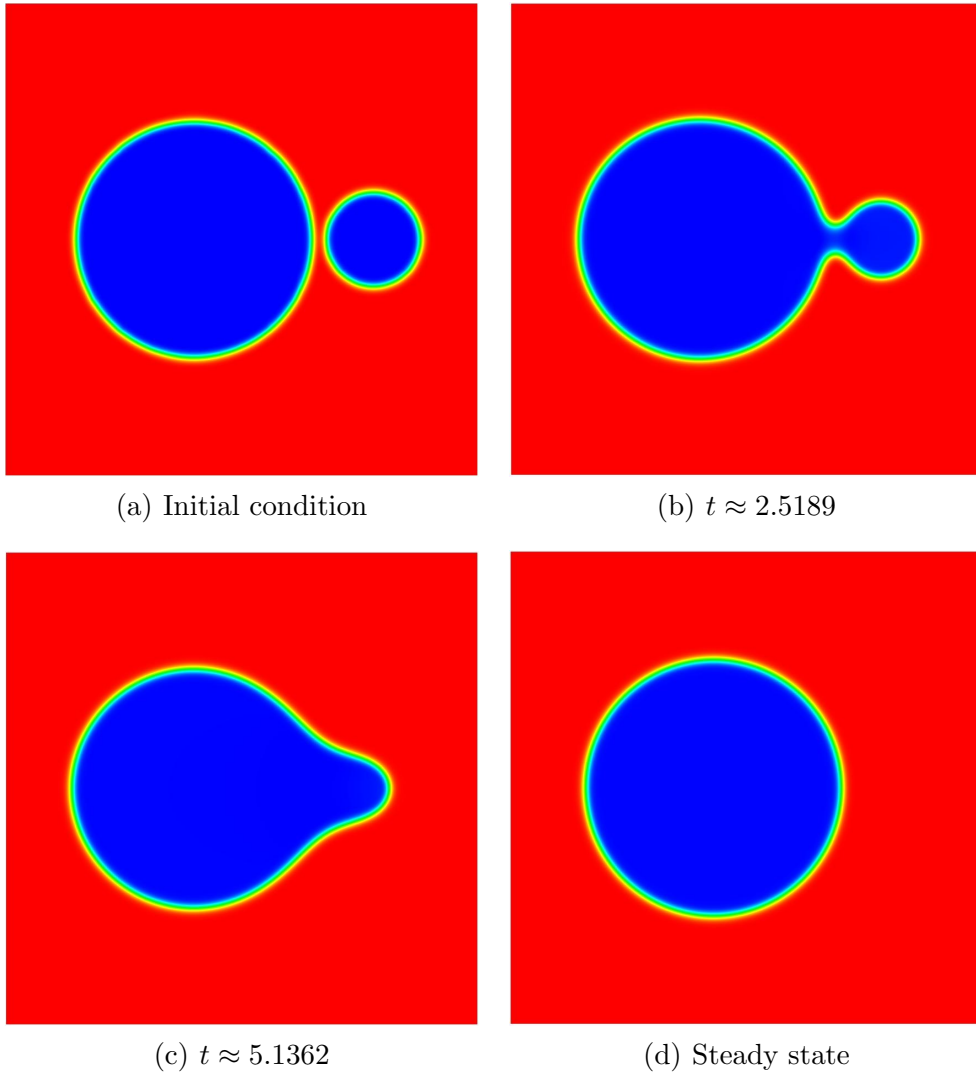
(a) Initial condition

(b) $t \approx 2.5189$

(c) $t \approx 5.1362$

(d) Steady state

Fig. 10. Coalescence of two vapor bubbles. Evolution of the density. The mesh is comprised of 256^2 $\mathcal{C}^1$-quadratic elements.

the capillarity number, and, as a consequence, it is the same in the two previous numerical examples (sections 5.1 and 5.2). Therefore, the Young-Laplace equation mandates

$$\Delta p_1 R_1 = \Delta p_2 R_2 \qquad (46)$$

where Δp_1 and Δp_2 are, respectively, the pressure difference between the vapor and liquid phases in the first and second numerical examples and R_1, R_2 are their corresponding bubble radii. In a diffuse interface representation of the liquid-vapor flow we need some procedure to define the radii of the bubbles. We define the boundary of the bubble as the set of points where the pressure takes on the value 0.353 (approximately the average of the maximum and minimum values taken by the density). Then, we fit a circumference to those points utilizing a least squares

24

(a) Initial condition

(b) $t \approx 2.5189$

(c) $t \approx 5.1362$

(d) Steady state

| 0.00184 | 0.0124 | 0.0177 | 0.0230 |
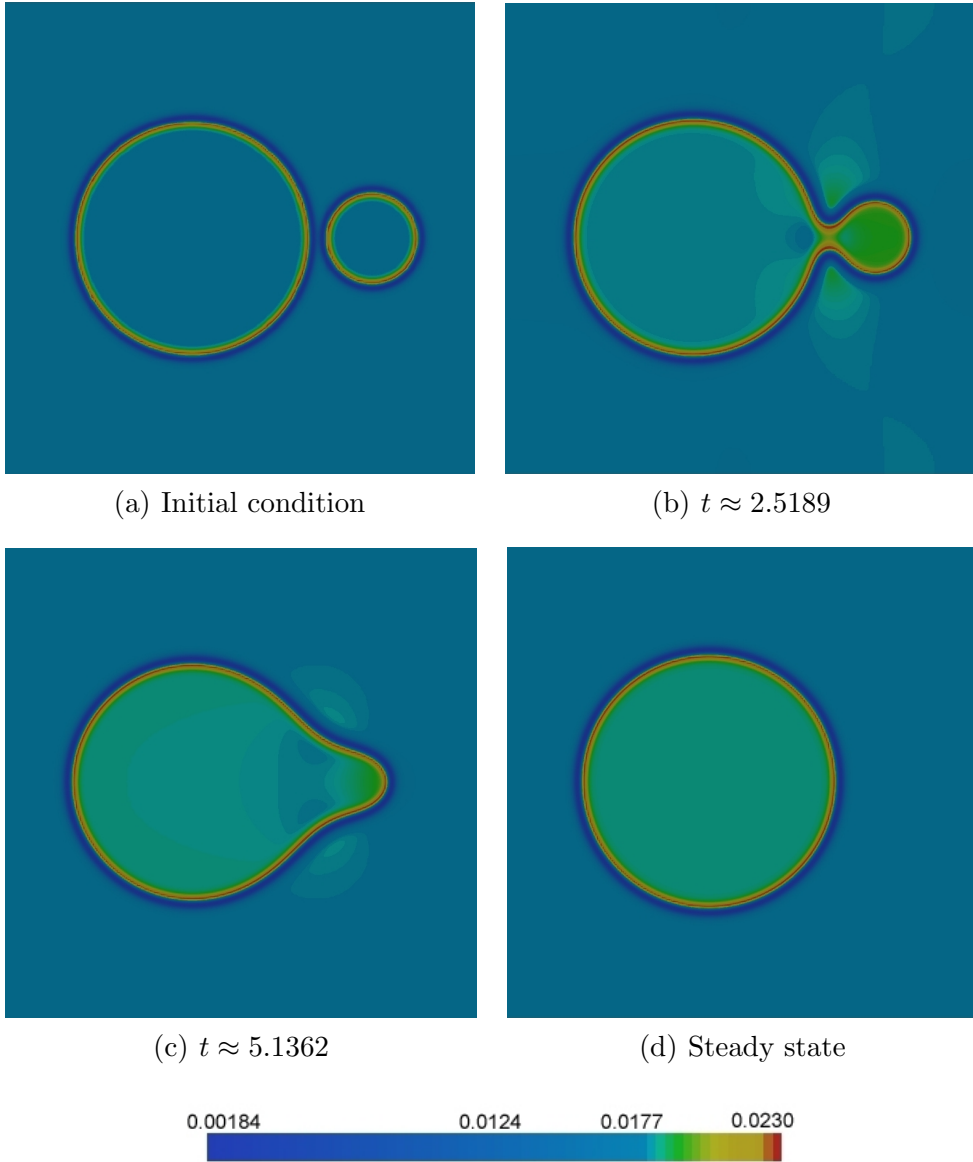
Fig. 11. Coalescence of two vapor bubbles. Evolution of the pressure. The mesh is comprised of 256^2 $\mathcal{C}^1$-quadratic elements.

approximation. Using this procedure in the two previous examples, we obtained

$$\Delta p_1 \approx 6.594 \cdot 10^{-4}; \quad \Delta p_2 \approx 4.820 \cdot 10^{-4}; \quad R_1 \approx 0.19835; \quad R_2 \approx 0.27140 \tag{47}$$

which implies that the Young-Laplace equation is satisfied with a relative error of approximately $1.74 \cdot 10^{-4}$.
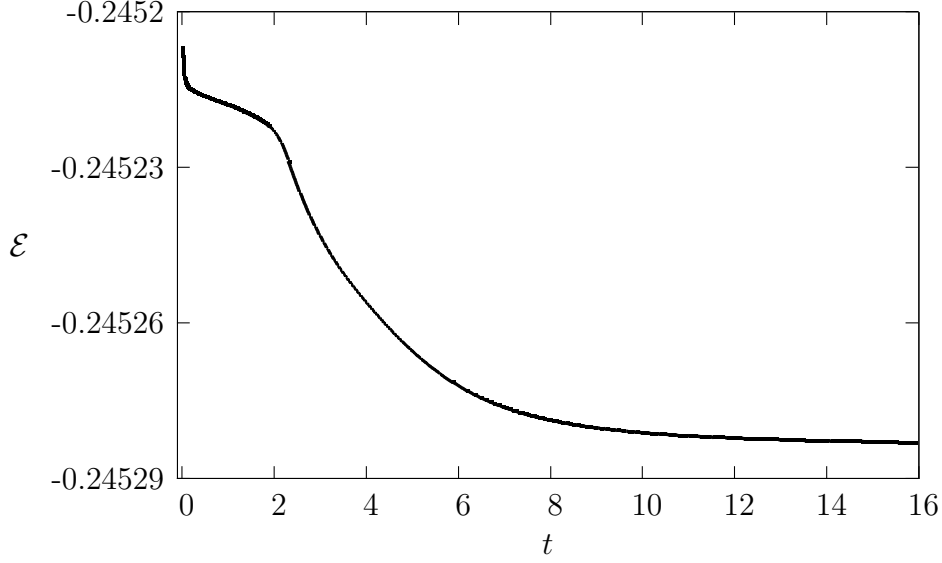
Fig. 12. Coalescence of two vapor bubbles. Evolution of the free energy. There is a significant variation of the free energy that corresponds to the time at which the two bubbles merge. The free energy is decreasing for all times. The mesh is comprised of 256^2 $\mathcal{C}^1$-quadratic elements.
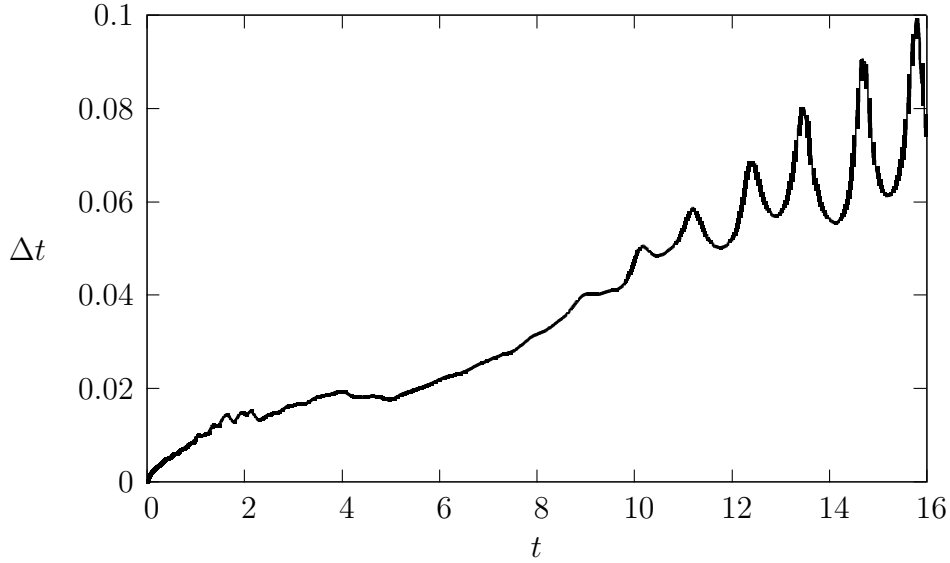
Fig. 13. Coalescence of two vapor bubbles. Evolution of the time step. The mesh is comprised of 256^2 $\mathcal{C}^1$-quadratic elements.

5.3 Evolution to static equilibrium in three dimensions

This example is the three dimensional counterpart of that presented in section 5.1. Our computational domain is $\overline{\Omega} = [0,1]^3$. At the initial time, we set three vapor bubbles with centers at points $C_1 = (0.75, 0.50, 0.25)$, $C_2 = (0.30, 0.50, 0.50)$ and $C_3 = (0.40, 0.75, 0.70)$. The radii of the bubbles are

26

$R_1 = 0.10$, $R_2 = 0.20$ and $R_3 = 0.08$, respectively. We regularize the interfaces using hyperbolic tangent profiles. Thus, for the density we take the initial condition

$$\rho_0(\boldsymbol{x}) = -0.15 + 0.25 \left[\tanh\left(\frac{d_1(\boldsymbol{x}) - R_1}{2\mathrm{Ca}} \right) + \tanh\left(\frac{d_2(\boldsymbol{x}) - R_2}{2\mathrm{Ca}} \right) + \tanh\left(\frac{d_3(\boldsymbol{x}) - R_3}{2\mathrm{Ca}} \right) \right] \tag{48}$$

with the usual notation. The velocity is zero at the initial time.

In Figure 14 we plot the evolution of the density in time. The physical process is the same as in section 5.1. In Figure 15 we plot isosurfaces of density for two different times. We also plot the streamlines from the center of the three bubbles. The color of the streamlines and the boundaries represents velocity magnitude.

In Figure 16 we plot the evolution of the free energy, which is decreasing at all times. The two main physical events that take place in this simulation, namely, the disappearance of two vapor bubbles, occur at the times when the time step size is reduced by our algorithm (see Figure 17).

Remark:

Since we are assuming that the temperature is constant, the isosurfaces of density may also be thought of as isosurfaces of entropy or pressure.

5.4 Coalescence of two bubbles in three dimensions

This example is the three dimensional counterpart of that presented in section 5.2. Our computational domain is $\overline{\Omega} = [0, 1]^3$. At the initial time, we set two vapor bubbles with centers at points $C_1 = (0.40, 0.50, 0.60)$, $C_2 = (0.75, 0.50, 0.50)$. The radii of the bubbles are $R_1 = 0.25$, $R_2 = 0.10$, respectively. We regularize the interfaces using hyperbolic tangent profiles. Thus, for the density we take the initial condition

$$\rho_0(\boldsymbol{x}) = 0.10 + 0.25 \left[\tanh\left(\frac{d_1(\boldsymbol{x}) - R_1}{2\mathrm{Ca}} \right) + \tanh\left(\frac{d_2(\boldsymbol{x}) - R_2}{2\mathrm{Ca}} \right) \right] \tag{49}$$

with the usual notation. The velocity is zero at the initial time.

In Figure 18 we plot the evolution of the density in time. The physical process is the same as in section 5.2. In Figure 19 we plot isosurfaces of density for two different times. We also plot the streamlines from the center of the two bubbles. The color of the streamlines and the boundaries represents velocity magnitude.

(a) Initial condition   (b) $t \approx 0.81012$
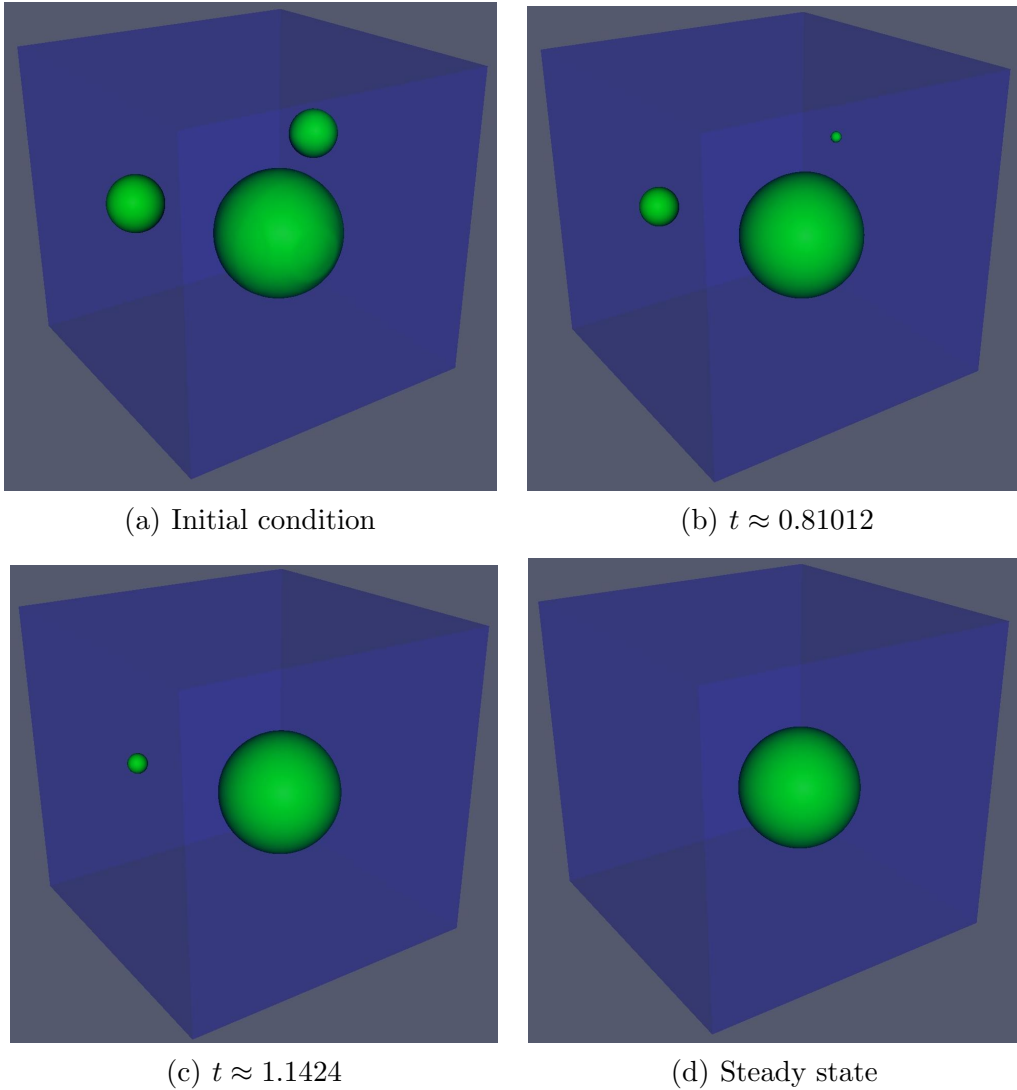
(c) $t \approx 1.1424$ (d) Steady state

Fig. 14. Static equilibrium in three dimensions. Evolution of the density from an initial condition with three vapor bubbles. The mesh is comprised of 128^3 $\mathcal{C}^1$ quadratic elements.

In Figure 20 and 21 we plot the evolution in time of the free energy and the time step, respectively.

6   Conclusions and future developments

This paper deals with the numerical simulation of the Navier-Stokes-Korteweg equations, a phase-field representation of water/water-vapor two-phase flow. We have developed a numerical formulation based on isogeometric analysis. Our formulation permits straightforward treatment of the third-order partial-differential operator that represents capillarity.
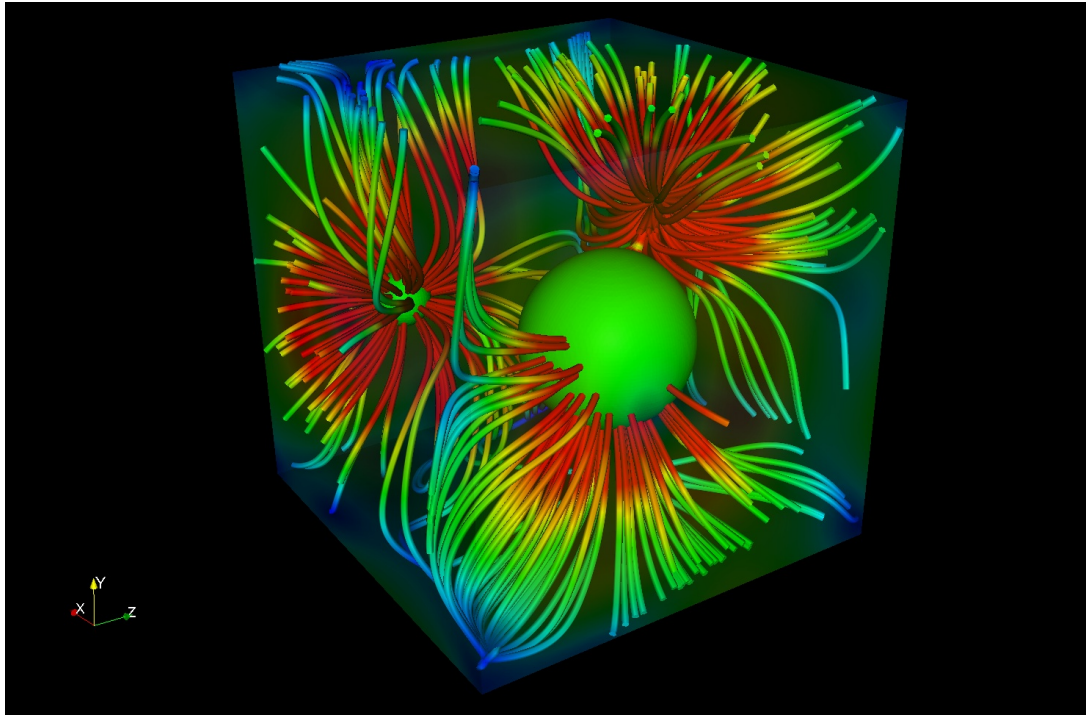
(a) $t \approx 0.81012$
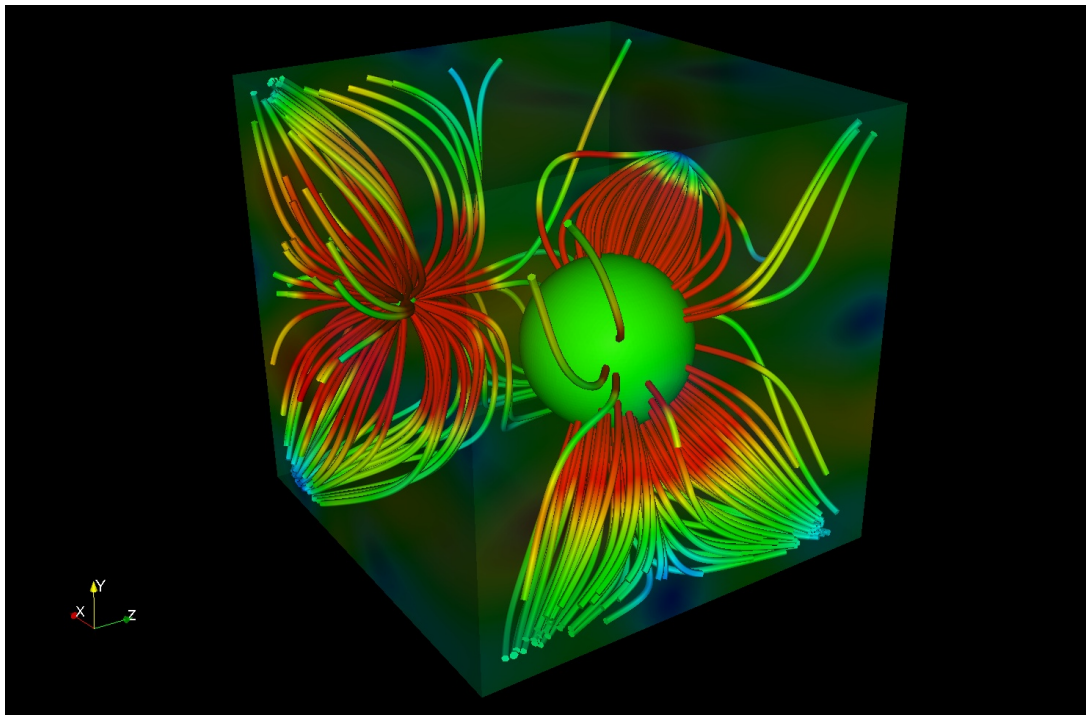
(b) $t \approx 1.1424$

Fig. 15. Static equilibrium in three dimensions. We represent streamlines from the center of the three vapor bubbles and isosurfaces of density. The color of the streamlines and the boundaries represents velocity magnitude. The mesh is comprised of 128^3 $\mathcal{C}^1$ quadratic elements.
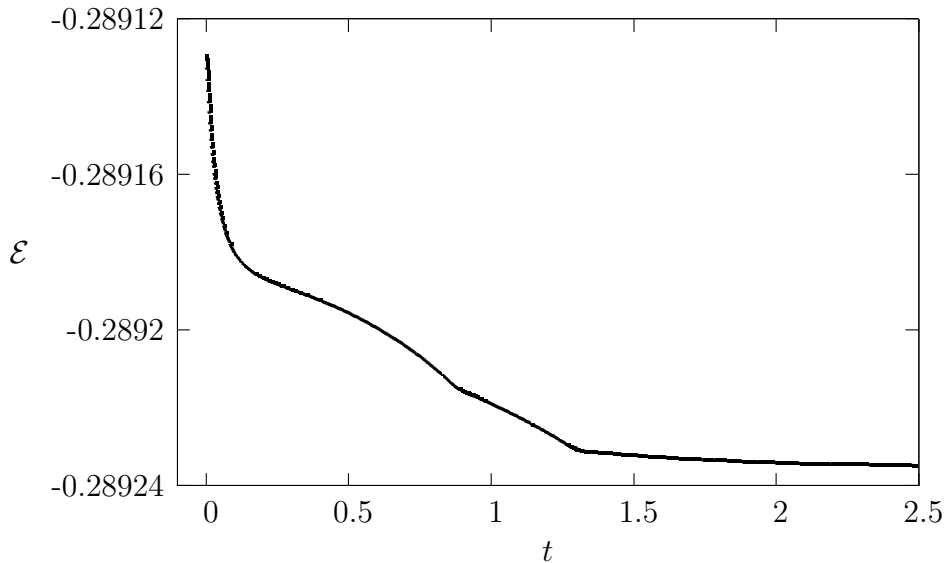
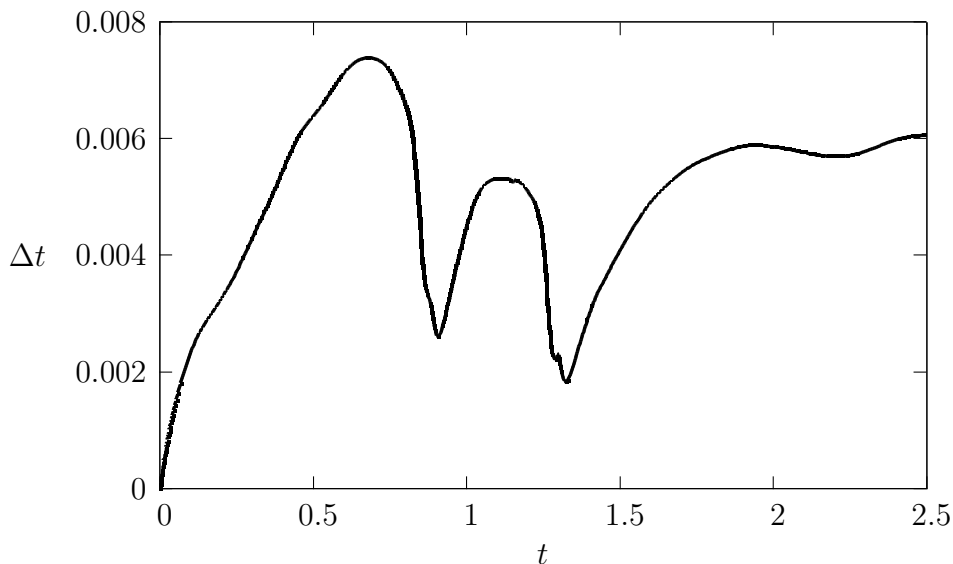Fig. 16. Static equilibrium in three dimensions. Evolution of the free energy. The mesh is comprised of 128^3 $\mathcal{C}^1$-quadratic elements.

Fig. 17. Static equilibrium in three dimensions. Evolution of the time step. There are two significant variations that correspond to the times at which the smaller bubbles vanish. The mesh is comprised of 128^3 $\mathcal{C}^1$-quadratic elements.

We have also introduced a new refinement methodology that desensitizes the numerical solution to the computational mesh. Using this technique we found a consistent and significant improvement over the standard methodology.

Finally, we have presented several numerical examples in two and three dimensions, which illustrate the effectiveness and robustness of our numerical formulation.
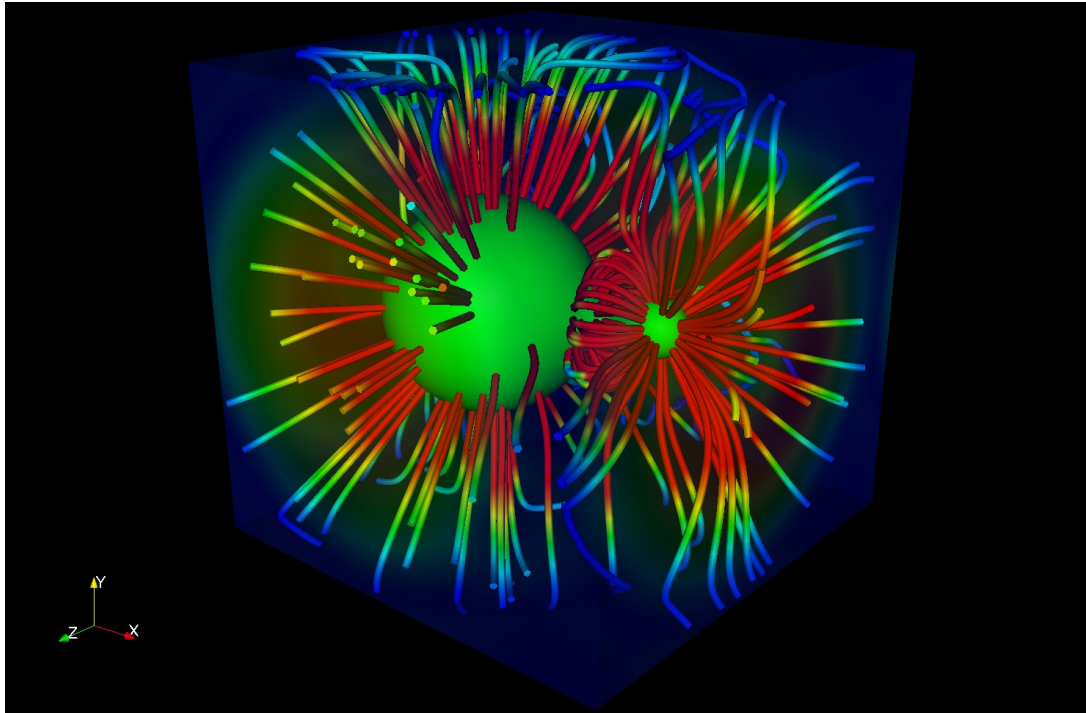
(a) Initial condition   (b) $t \approx 0.53500$

(c) $t \approx 1.4654$ (d) Steady state
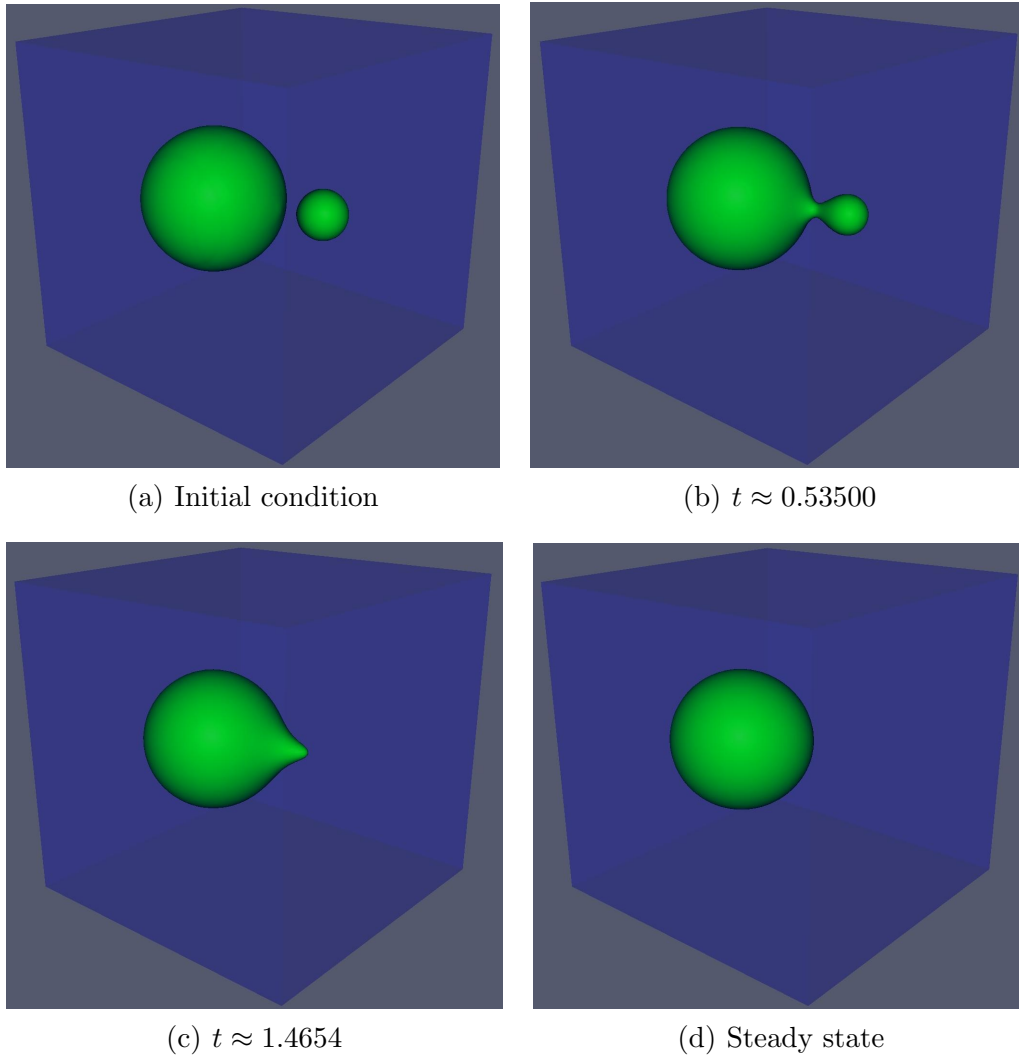
Fig. 18. Coalescence of two bubbles in three dimensions. Evolution of the density. The mesh is comprised of 128^3 $\mathcal{C}^1$ quadratic elements.

From the point of view of applications, future efforts should be devoted to the development of a generalized theory for air/water/water-vapor flows, which may be applicable to water mists used to fight fires. From the mathematical point of view, we believe that the Navier-Stokes-Korteweg equations may be generalized so that they reflect the difference between the viscosity of water and water-vapor.

7 Acknowledgements

31

(a) $t \approx 0.53500$
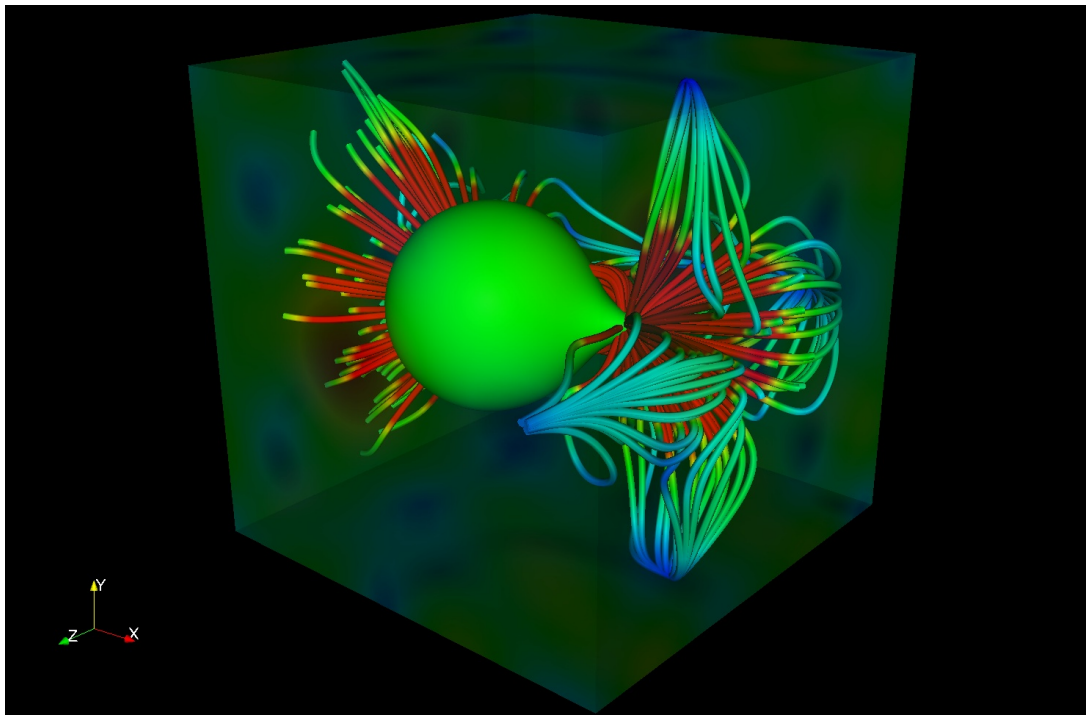
(b) $t \approx 1.4654$

Fig. 19. Coalescence of two bubbles in three dimensions. We represent streamlines from the center of the two vapor bubbles and isosurfaces of density. The color of the streamlines and the boundaries represents velocity magnitude. The mesh is comprised of 128^3 $\mathcal{C}^1$ quadratic elements.
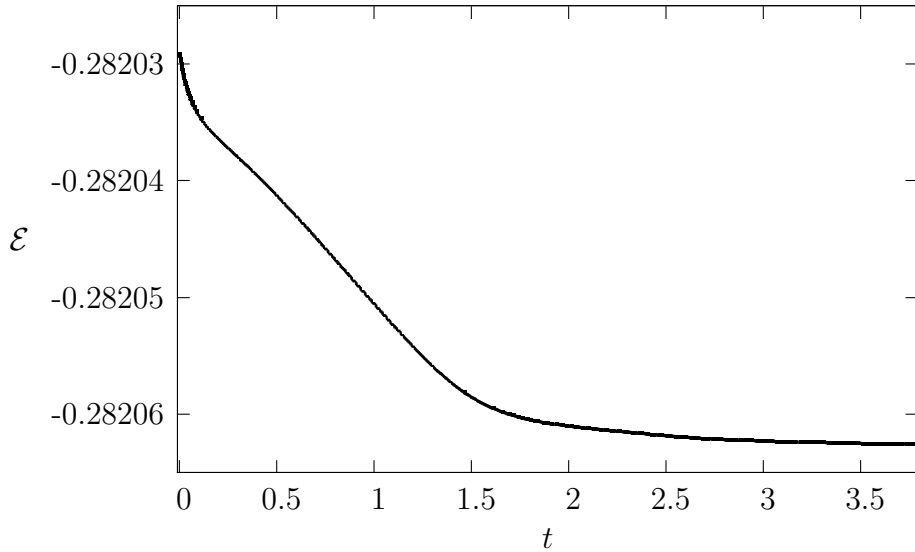
32

Fig. 20. Coalescence of two bubbles in three dimensions. Evolution of the free energy. The mesh is comprised of 128^3 $\mathcal{C}^1$-quadratic elements.
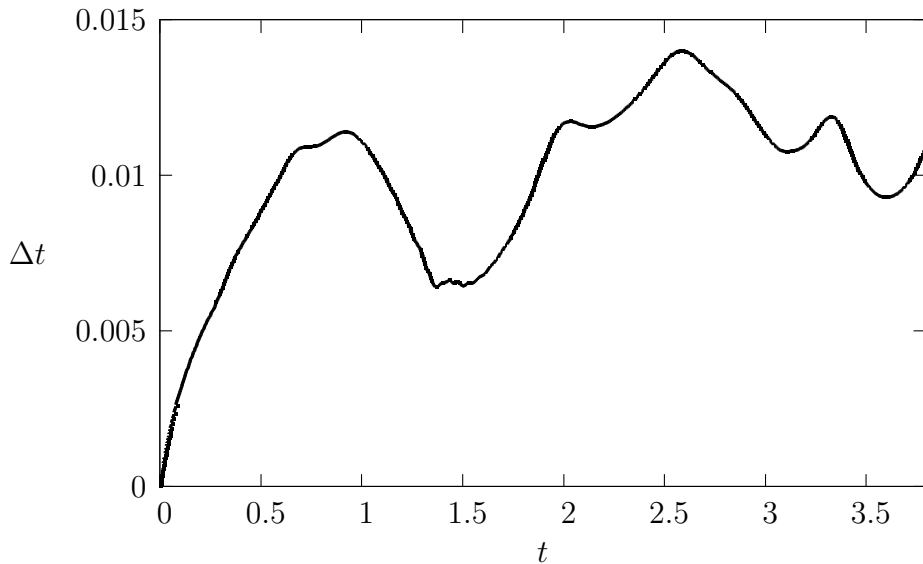

Fig. 21. Coalescence of two bubbles in three dimensions. Evolution of the time step. The mesh is comprised of 128^3 $\mathcal{C}^1$-quadratic elements.

33

MCA07S032, for the computational time.

References

[1] D.M. Anderson, G.B. McFadden, A.A. Wheeler, Diffuse-interface methods in fluid mechanics, *Annu. Rev. Fluid Mech.* **30** (1998) 139–165.

[2] I. Akkerman, Y. Bazilevs, V. M. Calo, T. J. R. Hughes, S. Hulshoff, The role of continuity in residual-based variational multiscale modeling of turbulence, *Computational Mechanics* **41** (2007) 371–378.

[3] G.I. Barenblatt, *Scaling, self-similarity, and intermediate asymptotics*, Cambridge University Press, 1996.

[4] D.J. Berthelot, *Journal of Physics* **8** 263 (1899).

[5] G.K. Batchelor, *An introduction to fluid dynamics*, Cambridge University Press, 1967.

[6] Y. Bazilevs, T.J.R. Hughes, NURBS-based isogeometric analysis for the computation of flows about rotating components, *Computational Mechanics* **43** (2008) 143–150.

[7] Y. Bazilevs, V.M. Calo, J.A. Cottrell, J.A. Evans, T.J.R. Hughes, S. Lipton, M.A. Scott, T.W. Sederberg, Isogeometric Analysis using T-splines, *Computer Methods in Applied Mechanics and Engineering*, **199** (2010) 229–263.

[8] Y. Bazilevs, V.M. Calo, J.A. Cottrell, T.J.R. Hughes, A. Reali, G. Scovazzi, Variational multiscale residual-based turbulence modeling for large eddy simulation of incompressible flows, *Computer Methods in Applied Mechanics and Engineering* **197** (2007) 173–201.

[9] A.J. Bray, Theory of phase ordering kinetics, *Advances in Physics* **43** (1994) 357–459.

[10] A. Buffa, G. Sangalli, R. Vázquez, Isogeometric analysis in electromagnetics: B-splines approximation, *Computer Methods in Applied Mechanics and Engineering*, in press.

[11] G. Caginalp, Stefan and Hele Shaw type models as asymptotic limits of the phase field equations, *Phys. Rev. A* **39** (1989) 5887–5896.

[12] V.P. Carey, *Liquid-vapor phase-change phenomena: An introduction to the thermophysics of vaporization and condensation processes in heat transfer equipment*, Taylor and Francis, 2008.

[13] J.W. Cahn, J.E. Hilliard, Free energy of a non-uniform system. I. Interfacial free energy, *The Journal of Chemical Physics* **28** (1958) 258–267.

[14] J.W. Cahn, J.E. Hilliard, Free energy of a non-uniform system. III. Nucleation in a two-component incompressible fluid, *The Journal of Chemical Physics* **31** (1959) 688–699.

[15] L. Cueto-Felgueroso, R. Juanes, Nonlocal interface dynamics and pattern formation in gravity-driven unsaturated flow through porous media, *Physical Review Letters* **101** (2008) 244504.

[16] L. Cueto-Felgueroso, R. Juanes, A phase-field model of unsaturated flow, *Water Resources Research*, **45** W10409 (2009).

[17] L.Q. Chen, Phase-field models for microstructural evolution, *Ann. Rev. Mater. Res.* **32** (2002) 113–140.

[18] J. Chung, G.M. Hulbert, A time integration algorithm for structural dynamics with improved numerical dissipation: The generalized-α method, *Journal of Applied Mechanics* **60** (1993) 371–375.

[19] J.A. Cottrell, T.J.R. Hughes, A. Reali, Studies of refinement and continuity in isogeometric structural analysis, *Computer Methods in Applied Mechanics and Engineering*, **196** (2007) 4160–4183.

[20] W. Craig Carter, J. E. Taylor, J. W. Cahn, Variational methods for microstructural-evolution theories, *JOM Journal of the Minerals, Metals and Materials Society* **49** (1997) 30–36.

[21] J. Crank, *Free and moving boundary problems*, Oxford Univerrsity Press, 1997.

[22] R. Danchin, B. Desjardins, Existence of solutions for compressible fluid models of Korteweg type. *Annales de l'institut Henri Poincaré (C) Analyse non linéaire*, **18** (2001) 97–133.

[23] D. Diehl, Higher order schemes for simulation of compressible liquid-vapor flows with phase change, PhD Thesis, 2007.

[24] J.E. Dunn, J. Serrin, On the thermomechanics of interstitial working, *Archives for Rational Mechanics and Analysis* **88** (1985) 95–133.

[25] J.A. Evans, Y. Bazilevs, I. Babuška, T.J.R. Hughes, n-Widths, supinfs, and optimality ratios for the k-version of the isogeometric finite element method, *Computer Methods in Applied Mechanics and Engineering*, **198** (2009) 1726–1741.

[26] D.N. Fan, L.Q. Chen, Diffuse interface description of grain boundary motion, *Philosophical Magazine Letters* **75** (1997) 187–196.

[27] I. Fonseca, M. Morini, Surfactants in foam stability: A phase field model, *Arch. Ration. Mech.* **183** (2007) 411-456

[28] H.B. Frieboes, J.S. Lowengrub, S. Wise, X. Zheng, P. Macklin, E.L. Bearer, V. Cristini, Computer simulation of glioma growth and morphology, *NeuroImage* **37** (2007) 59–70.

[29] E. Fried, M.E. Gurtin, Dynamic solid-solid transitions with phase characterized by an order parameter, *Phys. D*, **72** (1994) 287–308.

[30] H. Garcke, B. Nestler, A mathematical model for grain growth in thin metallic films, *Math. Models Methods Appl. Sci.* **10** (2000) 895–921.

[31] H. Garcke, B. Nestler, B. Stoth, On anisotropic order parameter models for multiphase systems and their sharp interface limits, *Phys. D* **115** (1998) 87–108.

[32] H. Garcke, A. Novick-Cohen, A singular limit for a system of degenerate Cahn-Hilliard equations, *Adv. Differential equations* **5** (2000) 401–434.

[33] P.G. Gennes, F. Brochard-Wyart, D. Quere, *Capillarity and Wetting Phenomena: Drops, Bubbles, Pearls, Waves*, Springer, 2002.

[34] W. Gibbs, On the Equilibrium of Heterogeneous Substances, *Transactions of the Connecticut Academy* (1876) 108–248, 343–534.

[35] H. Gomez, V.M. Calo, Y. Bazilevs, T.J.R. Hughes, Isogeometric analysis of the Cahn-Hilliard phase-field model, *Computer Methods in Applied Mechanics and Engineering* **197** (2008) 4333–4352.

[36] H. Gomez, V.M. Calo, T.J.R. Hughes, Isogeometric Analysis of Phase-Field Models: Application to the Cahn-Hilliard Equation, *Computational Methods in Applied Sciences*, Springer Verlag, (2009) 1–16.

[37] B.T. Hayes, P.G. LeFloch, Nonclasical shocks and kinetic relations. Finite difference schemes, *SIAM Journal Numerical Analysis* **35** (1998) 2169–2194.

[38] J.E. Huber, N.A. Fleck, C.M. Landis, R.M. McMeeking, A constitutive model for ferroelectric polycrystals, *Journal of the Mechanics and Physics of Solids* **47** (2009) 1663–1697.

[39] T.J.R. Hughes, *The Finite Element Method: Linear Static and Dynamic Finite Element Analysis*, Dover Publications, Mineola, NY, 2000.

[40] T.J.R. Hughes, J.A. Cottrell, Y. Bazilevs, Isogeometric analysis: CAD, finite elements, NURBS, exact geometry and mesh refinement, *Computer Methods in Applied Mechanics and Engineering*, **194** (2005) 4135–4195.

[41] T.J.R. Hughes, A. Reali, G. Sangalli, Duality and unified analysis of discrete approximations in structural dynamics and wave propagation: Comparison of p-method finite elements with k-method NURBS, *Computer Methods in Applied Mechanics and Engineering*, **197** (2008) 4104–4124.

[42] D. Jamet, The second gradient method for the direct numerical simulation of liquid-vapor flows with phase change, *Journal of Computational Physics* **169** (2001) 624–651.

[43] D. Jamet, D. Torres, J.U. Brackbill, On the theory and computation of surface tension: The elimination of parasitic currents through energy conservation in the second-gradient method, *Journal of Computational Physics* **182** (2002) 262–276.

[44] K.E. Jansen, C.H. Whiting, G.M. Hulbert, A generalized-α method for integrating the filtered Navier-Stokes equations with a stabilized finite element method, *Computer Methods in Applied Mechanics and Engineering*, **190** (1999) 305–319.

[45] J.-H. Jeong, N. Goldenfeld, J. A. Dantzig, Phase field model for three-dimensional dendritic growth with fluid flow, *Physical Review E* **64** (2001) 1–14

[46] Y-T. Kim, N. Provatas, N. Goldenfeld, J. A. Dantzig, Universal Dynamics of Phase Field Models for Dendritic Growth, *Physical Review E* **59** (1999) 2546–2549.

[47] R. Kobayashi, A numerical approach to three-dimensional dendritic solidification, *Experimental Mathematics* **3** (1994).

[48] D.J. Korteweg, Sur la forme que prennent les équations du mouvement des fluids si l'on tient compte des forces capillaires causés par les variations de densité, *Archives Néerlandaises des Sciences Exactes et naturelles* **6** (1901) 1–24.

[49] L.D. Landau, V.I. Ginzburg, On the theory of superconductivity, in *Collected papers of L.D. Landau*, D. ter Haar, ed., Pergamon Oxford (1965) 626–633.

[50] C.M. Landis, Fully coupled multi-axial, symmetric constitutive laws for polycristalline ferroelectric ceramics, *Journal of the Mechanics and Physics of Solids* **50** (2002) 127–152.

[51] P.G. LeFloch, M. Mohammadian, Why many theories of shock waves are necessary: Kinetic functions, equivalent equations, and fourth-order models, *Journal of Computational Physics* **227** (2008) 4162–4189.

[52] J. Lighthill, *Waves in fluids*, Cambridge University Press, 1978.

[53] S. Lipton, J.A. Evans, Y. Bazilevs, T. Elguedj, T.J.R. Hughes, Robustness of isogeometric structural discretizations under severe mesh distortion, *Computer Methods in Applied Mechanics and Engineering*, **199** (2010) 357–373.

[54] J. Lowengrub, L. Truskinovsky, Quasi-incompressible Cahn-Hilliard fluids and topological transitions, *Proc. Roy. Soc. London Ser. A* **454** (1998) 2617–2654.

[55] O. Penrose, P.C. Fife, Thermodynamically consistent models of phase field type for the kinetics of phase transition, *Phys. D* **43** (1990) 44–62.

[56] Y. Saad, M.H. Schultz, GMRES: A generalized minimal residual algorithm for solving nonsymmetric linear systems, *SIAM Journal of Scientific and Statistical Computing* **7** (1986) 856–869.

[57] J. Serrin, The area rule for simple fluid phase transitions, *Journal of Elasticity* **90** (2008) 129–159.

[58] R.H. Stogner, G.F. Carey, $\mathcal{C}^1$ macroelements in adaptive finite element methods, *International Journal for Numerical Methods in Engineering* **70** (2007) 1076-1095.

[59] R.H. Stogner, G.F. Carey, B.T. Murray, Approximation of Cahn-Hilliard diffuse interface models using parallel adaptive mesh refinement and coarsening with C1 elements, *International Journal for Numerical Methods in Engineering* **76** 636–661.

[60] S. Tremaine, On the origin of irregular structure in Saturn's rings, *Astronomical Journal* **125** (2003) 894–901.

[61] J.D. van der Waals, The thermodynamis theory of capillarity under the hypothesis of a continuous variation of density, *J. Stat. Phys.* **20** (1979) 197–244.

[62] A.H. Wilson, Thermodynamics and statistical mechanics, Cambridge University Press, 1957.